

The Supernova Legacy Survey: measurement of Ω_M , Ω_Λ and w from the first year data set^{★,★★}

P. Astier¹, J. Guy¹, N. Regnault¹, R. Pain¹, E. Aubourg^{2,3}, D. Balam⁴, S. Basa⁵, R. G. Carlberg⁶, S. Fabbro⁷, D. Fouchez⁸, I. M. Hook⁹, D. A. Howell⁶, H. Lafoux³, J. D. Neill⁴, N. Palanque-Delabrouille³, K. Perrett⁶, C. J. Pritchett⁴, J. Rich³, M. Sullivan⁶, R. Taillet^{1,10}, G. Aldering¹¹, P. Antilogus¹, V. Arsenijevic⁷, C. Balland^{1,2}, S. Baumont^{1,12}, J. Bronder⁹, H. Courtois¹³, R. S. Ellis¹⁴, M. Filiol⁵, A. C. Gonçalves¹⁵, A. Goobar¹⁶, D. Guide¹, D. Hardin¹, V. Lisset³, C. Lidman¹², R. McMahon¹⁷, M. Mouchet^{15,2}, A. Mourao⁷, S. Perlmutter^{11,18}, P. Ripoche⁸, C. Tao⁸, and N. Walton¹⁷

(Affiliations can be found after the references)

Received 9 September 2005 / Accepted 11 October 2005

ABSTRACT

We present distance measurements to 71 high redshift type Ia supernovae discovered during the first year of the 5-year Supernova Legacy Survey (SNLS). These events were detected and their multi-color light-curves measured using the MegaPrime/MegaCam instrument at the Canada-France-Hawaii Telescope (CFHT), by repeatedly imaging four one-square degree fields in four bands, as part of the CFHT Legacy Survey (CFHTLS). Follow-up spectroscopy was performed at the VLT, Gemini and Keck telescopes to confirm the nature of the supernovae and to measure their redshift. With this data set, we have built a Hubble diagram extending to $z = 1$, with all distance measurements involving at least two bands. Systematic uncertainties are evaluated making use of the multi-band photometry obtained at CFHT. Cosmological fits to this first year SNLS Hubble diagram give the following results: $\Omega_M = 0.263 \pm 0.042$ (*stat*) ± 0.032 (*sys*) for a flat Λ CDM model; and $w = -1.023 \pm 0.090$ (*stat*) ± 0.054 (*sys*) for a flat cosmology with constant equation of state w when combined with the constraint from the recent Sloan Digital Sky Survey measurement of baryon acoustic oscillations.

Key words. supernovae: general – cosmology: observations – cosmological parameters

1. Introduction

The discovery of the acceleration of the Universe stands as a major breakthrough of observational cosmology. Surveys of cosmologically distant Type Ia supernovae (SNe Ia; Riess et al. 1998; Perlmutter et al. 1999) indicated the presence of a new, unaccounted-for “dark energy” that opposes the self-attraction of matter and causes the expansion of the Universe to accelerate. When combined with indirect measurements using cosmic microwave background (CMB) anisotropies, cosmic shear and studies of galaxy clusters, a cosmological world model has emerged that describes the Universe as flat, with about 70% of its energy contained in the form of this cosmic dark energy (see for example Seljak et al. 2005).

Current projects aim at directly probing the nature of the dark energy via a determination of its equation of state parameter – the pressure to energy-density ratio – $w \equiv p_X/\rho_X$, which also defines the time dependence of the dark energy density: $\rho_X \sim a^{-3(1+w)}$, where a is the scale factor. Recent constraints

and Space Administration. The Observatory was made possible by the generous financial support of the W.M. Keck Foundation.

★ Tables 7–9 are only available in electronic form at <http://www.edpsciences.org>

* Based on observations obtained with MegaPrime/MegaCam, a joint project of CFHT and CEA/DAPNIA, at the Canada-France-Hawaii Telescope (CFHT) which is operated by the National Research Council (NRC) of Canada, the Institut National des Sciences de l’Univers of the Centre National de la Recherche Scientifique (CNRS) of France, and the University of Hawaii. This work is based in part on data products produced at the Canadian Astronomy Data Centre as part of the Canada-France-Hawaii Telescope Legacy Survey, a collaborative project of NRC and CNRS. Based on observations obtained at the European Southern Observatory using the Very Large Telescope on the Cerro Paranal (ESO Large Programme 171.A-0486). Based on observations (programs GN-2004A-Q-19, GS-2004A-Q-11, GN-2003B-Q-9, and GS-2003B-Q-8) obtained at the Gemini Observatory, which is operated by the Association of Universities for Research in Astronomy, Inc., under a cooperative agreement with the NSF on behalf of the Gemini partnership: the National Science Foundation (USA), the Particle Physics and Astronomy Research Council (UK), the National Research Council (Canada), CONICYT (Chile), the Australian Research Council (Australia), CNPq (Brazil) and CONICET (Argentina). Based on observations obtained at the W.M. Keck Observatory, which is operated as a scientific partnership among the California Institute of Technology, the University of California and the National Aeronautics

on w (Knop et al. 2003; Tonry et al. 2003; Barris et al. 2004; Riess et al. 2004) are consistent with a very wide range of Dark Energy models. Among them, the historical cosmological constant ($w = -1$) is 10^{120} to 10^{60} smaller than plausible vacuum energies predicted by fundamental particle theories. It also cannot explain why matter and dark energy have comparable densities today. ‘‘Dynamical Λ ’’ models have been proposed (quintessence, k-essence) based on speculative field models, and some predict values of w above -0.8 – significantly different from -1 . Measuring the average value of w with a precision better than 0.1 will permit a discrimination between the null hypothesis (pure cosmological constant, $w = -1$) and some dynamical dark energy models.

Improving significantly over current SN constraints on the dark energy requires a ten-fold larger sample (i.e. ~ 1000) at $0.2 < z < 1.$, where w is best measured), in order to significantly improve on statistical errors but also, most importantly, on systematic uncertainties. The traditional method of measuring distances to SNe Ia involves different types of observations at about 10 different epochs spread over nearly 3 months: discovery via image subtraction, spectroscopic identification, and photometric follow-up, usually on several telescopes. Many objects are lost or poorly measured in this process due to the effects of inclement weather during the follow-up observations, and the analysis often subject to largely unknown systematic uncertainties due to the use of various instruments and telescopes.

The Supernova Legacy Survey (SNLS)¹ was designed to improve significantly over the traditional strategy as follows: 1) discovery and photometric follow-up are performed with a wide field imager used in ‘‘rolling search’’ mode, where a given field is observed every third to fourth night as long as it remains visible; 2) service observing is exploited for both spectroscopy and imaging, reducing the impact of bad weather. Using a single imaging instrument to observe the same fields reduces photometric systematic uncertainties; service observing optimizes both the yield of spectroscopic observing time, and the light-curve sampling.

In this paper we report the progress made, and the cosmological results obtained, from analyzing the first year of the SNLS. We present the data collected, the precision achieved both from improved statistics and better control of systematics, and the potential of the project to further reduce and control systematic uncertainties on cosmological parameters. Section 2 describes the imaging and spectroscopic surveys and their current status. Sections 3 and 4 present the data reduction and photometric calibration. The light-curve fitting method, the SNe samples and the cosmological analysis are discussed in Sect. 5. A comparison of the nearby and distant samples used in the cosmological analysis is performed in Sect. 6 and the systematic uncertainties are discussed in Sect. 7.

2. The Supernova Legacy Survey

The Supernova Legacy Survey is comprised of two components: an imaging survey to detect SNe and monitor their

Table 1. Coordinates and average Milky Way extinction (from Schlegel et al. 1998) of fields observed by the Deep/SN component of the CFHTLS.

Field	RA(2000)	Dec (2000)	$E(B - V)$ (MW)
D1	02:26:00.00	−04:30:00.0	0.027
D2	10:00:28.60	+02:12:21.0	0.018
D3	14:19:28.01	+52:40:41.0	0.010
D4	22:15:31.67	−17:44:05.0	0.027

light-curves, and a spectroscopic program to confirm the nature of the candidates and measure their redshift.

2.1. The imaging survey

The imaging is taken as part of the deep component of the CFHT Legacy Survey (CFHTLS 2002) using the one square degree imager, MegaCam (Boulade et al. 2003). In total, CFHTLS has been allocated 474 nights over 5 years and consists of 3 surveys: a very wide shallow survey (1300 square degrees), a wide survey (120 square degrees) and a deep survey (4 square degrees). The 4 pointings of the deep survey are evenly distributed in right ascension (Table 1). The observations for the deep survey are sequenced in a way suitable for detecting supernovae and measuring their light-curves: in every lunation in which a field is visible, it is imaged at five equally spaced epochs during a MegaCam run (which lasts about 18 nights). Observations are taken in a combination of r_M , i_M plus g_M or z_M filters (the MegaCam filter set; see Sect. 4) depending on the phase of the moon. Each field is observed for 5 to 7 consecutive lunations. Epochs lost to weather on any one night remain in the queue until the next clear observing opportunity, or until a new observation in the same filter is scheduled.

During the first year of the survey, the observing efficiency was lower than expected and the nominal observation plan could not always be fulfilled. The scheduled i_M exposures (3×3600 s plus 2×1800 s per lunation) and r_M exposures (5 epochs $\times 1500$ s) were usually acquired. Assigned a lower priority, g_M and z_M received less time than originally planned: on average only 2.2 epochs of 1050 s were collected per lunation in g_M , and 2 epochs of 2700 s in z_M ; for the latter, the average ignores the D2 field and the D3 field in 2003, for which only fragmentary observations were obtained in z_M . With efficiency ramping up, g_M and z_M approached their nominal rate in May 2004, and since then the nominal observation plan (detailed in Sullivan et al. 2005) is usually completed.

Observations and real-time pre-processing are performed by the CFHT staff using the Elixir reduction pipeline (Magnier & Cuillandre 2004), with the data products immediately available to the SN search teams. We have set up two independent real-time pipelines which analyze these pre-processed images. The detection of new candidates is performed by subtracting a ‘‘past’’ image to the current images, where the past-image is constructed by stacking previous observations of the same field. The key element of these pipelines is matching the point

¹ see <http://cfht.hawaii.edu/SNLS/>

spread function of a new exposure to the past-image. This is done using the Alard algorithm (Alard & Lupton 1998; Alard 2000) for one of the pipelines, and using a non-parametric approach for the other. New candidates are detected and measured on the subtraction images; detections are matched to other detections in the field, if any. One of the pipelines processes all bands on an equal footing, the other detects in the i_M band (which is deep enough for trigger purposes) and measures fluxes in the other bands. The two candidate lists are merged after each epoch and typically have an overlap greater than 90% for $i_M(AB) < 24.0$ after two epochs in a dark run. The reasons for one candidate being found by only one pipeline are usually traced to different masking strategies or different handling of the CCD overlap regions.

2.2. Spectroscopic follow-up

Spectroscopy is vital in order to obtain SN redshifts, and to determine the nature of each SN candidate. This requires observations on 8–10 m class telescopes due to the faintness of these distant supernovae. Spectroscopic follow-up time for the candidates presented in this paper was obtained at a variety of telescopes during the Spring and Fall semesters of 2003 and the Spring semester of 2004. The principle spectroscopic allocations were at the European Southern Observatory Very Large Telescope (program ID (171.A-0486); 60 h per semester), and at Gemini-North and South (Program-IDs: GN-2004A-Q-19, GS-2004A-Q-11, GN-2003B-Q-9, and GS-2003B-Q-8; 60 h per semester). Spectroscopic time was also obtained at Keck-I and Keck-II (3 nights during each Spring semester) as the D3 field cannot be seen by VLT or Gemini-South. Further complementary spectroscopic follow-up observations were also obtained at Keck-I (4 nights in each of 2003A, 2003B and 2004A) as part of a detailed study of the intermediate redshift SNe in our sample (Ellis et al., in prep.).

Most of the observations are performed in long-slit mode. The detailed spectroscopic classification of these candidates is discussed elsewhere (see Howell et al. 2005 and Basa et al., in prep.). In summary, we consider two classes of events (see Howell et al. 2005 for the exact definitions): secure SNe Ia events (“SN Ia”), and probable Ia events (“SN Ia*”), for which the spectrum matches a SN Ia better than any other type, but does not completely rule out other possible interpretations. All other events which were not spectroscopically identified as SN Ia or SN Ia* were ignored in this analysis.

The imaging survey still delivers more variable candidates than can actually be observed spectroscopically. Hence, an accurate ranking of these candidates for further observations is essential. This ranking is performed to optimize the SN Ia yield of our allocations. Our method uses both a photometric selection tool (discussed in Sullivan et al. 2005) which performs real-time light-curve fits to reduce the contamination of core-collapse SNe, and a database of every variable object ever detected by our pipelines to remove AGN and variable stars which are seen to vary repeatedly in long-timescale data sets (more than one year).

SN Ia candidates fainter than $i_M = 24.5$ (likely at $z > 1$) and those with very low percentage increases over their host galaxies (where identification is extremely difficult – see Howell et al. 2005) are usually not observed. With the real-time light-curve fit technique, approximately 70% of our candidates turned out to be SNe Ia. The possible biases associated with this selection were studied in Sullivan et al. (2005) and found to be negligible.

2.3. The first year data set

The imaging survey started in August 2003 after a few months of MegaCam commissioning. (Some SN candidates presented here were detected during the commissioning period.) This paper considers candidates with maximum light up to July 15th 2004, corresponding approximately to a full year of operation. During this time frame, which includes the ramping-up period of the CFHTLS, about 400 transients were detected, 142 spectra were acquired: 20 events were identified as Type II supernovae, 9 as AGN/QSO, 4 as SN Ib/c, and 91 events were classified as SN Ia or SN Ia*. The 18 remaining events have inconclusive spectra. Table 7 gives the 91 objects identified as SN Ia or SN Ia* during our first year of operation.

3. Data reduction

3.1. Image preprocessing

At the end of each MegaCam run, the images are pre-processed again at CFHT using the Elixir pipeline (Magnier & Cuillandre 2004). This differs from the real-time reduction process described in Sect. 2.1, in that master flat-field images and fringe-correction frames are constructed from all available data from the entire MegaCam run (including PI data). The Elixir process consists of flat-fielding and fringe subtraction, with an approximate astrometric solution also derived. Elixir provides reduced data which has a uniform photometric response across the mosaic (at the expense of a non-uniform sky background). This “photometric flat-field” correction is constructed using exposures with large dithers obtained on dense stellar fields.

The SNLS pipelines then associate a weight map with each Elixir-processed image (i.e. each CCD from a given exposure) from the flat-field frames and the sky background variations. Bad pixels (as identified by Elixir), cosmic rays (detected using the Laplacian filter of van Dokkum 2001), satellite trails, and saturated areas are set to zero in the weight maps. An object catalog is then produced using SExtractor (Bertin & Arnouts 1996), and point-like objects are used to derive an image quality (IQ) estimate. The sky background map computed by SExtractor is then subtracted from the image. We additionally perform aperture photometry on the objects of the SExtractor catalog for the purpose of photometric calibration (see Sect. 4).

3.2. Measurement of supernova fluxes

For each supernova candidate, the image with the best IQ (subsequently called “reference”) is identified, and all other images

(both science images and their weight maps) are resampled to the pixel grid defined by this reference. The variations of the Jacobian of the geometrical transformations, which translate into photometric non-uniformities in the re-sampled images, are sufficiently small (below the millimag level) to be ignored. We then derive the convolution kernels that would match the PSF (modeled using the DAOPHOT package Stetson 1987) of the reference image to the PSF of the other resampled science images, *but we do not perform the convolutions*. These convolution kernels not only match the PSFs, but also contain the photometric ratios of each image to the reference. We ensure that these photometric ratios are spatially uniform by imposing a spatially uniform kernel integral, but allow for spatial kernel shape variations as the images may have spatially varying PSFs. Following Alard (2000), the kernel is fit on several hundred objects selected for their high, though unsaturated, peak flux. The kernel fit is made more robust by excluding objects with large residuals and iterating.

Our approach to the differential flux measurement of a SN is to simultaneously fit all images in a given filter with a model that includes (i) a spatially variable galaxy (constant with time), and (ii) a time-variable point source (the supernova). The model is described in detail in Fabbro (2001). The shape of the galaxy and positions of both galaxy and supernova are fit globally. The intensity $D_{i,p}$ in a pixel p of image i is modeled as:

$$D_{i,p} = [(f_i P_{\text{ref}} + g) \otimes k_i]_p + b_i \quad (1)$$

where f_i are the supernova fluxes, P_{ref} is the PSF of the reference image centered on the SN position; k_i is the convolution kernel that matches the PSF of the reference image to the PSF of image i ; g is the intensity of the host galaxy in the reference image, and b_i is a local (sky) background in image i . The non parametric galaxy “model” g is made of independent pixels which represent the galaxy in the best IQ image. All fluxes (f_i) are expressed in units of the reference image flux.

The fit parameters are: the supernova position and the galaxy pixel values (common to all images), the supernova fluxes, and a constant sky background (different for each image). In some images in the series, the supernova flux is known to be absent or negligible; these frames enter the fit as “zero flux images” and are thus used to determine the values of the galaxy pixels. The least-squares photometric fit minimizes:

$$\chi^2 = \sum_{i,p} W_{i,p} (D_{i,p} - I_{i,p})^2 \quad (2)$$

where $I_{i,p}$ and $W_{i,p}$ are the image and weight values of pixel p in image i , and the sums run over all images that contain the SN position, and all pixels in the fitted stamp of this image.

Note that this method does not involve any real image convolution: the fitted model possesses the PSF of the reference image, and it is the model that is convolved to match the PSF of every other image. We typically fit 50×50 galaxy pixels and several hundred images, and each SN fit usually has 2000 to 3000 parameters. The fit is run once, 5σ outlier pixels are removed, and the fit is run again.

The photometric fit yields values of the fit parameters along with a covariance matrix. There are obvious correlations between SN fluxes and galaxy brightness, between these two parameters and the background level, and between the SN position and the flux, for any given image. More importantly, the uncertainty in the SN position and the galaxy brightness introduces correlations between fluxes at different epochs that have to be taken into account when analyzing the light-curves. Note that flux variances and the correlations between fluxes decrease when adding more “zero flux images” into the fit. It will therefore be possible to derive an improved photometry for most of the events presented in this paper, when the fields are observed again and more images without SN light are available.

3.3. Flux uncertainties

Once the photometric fit has converged, the parameter covariance matrix (including flux variances and covariances) is derived. This Section addresses the accuracy of these uncertainties, in particular the flux variances and covariances, which are used as inputs to the subsequent light-curve fit.

The normalization of the parameter covariance matrix directly reflects the normalization of image weights. We checked that the weights are on average properly normalized because the minimum χ^2 per degree of freedom is very close to 1 (we find 1.05 on average). However, this does not imply mathematically that the flux uncertainties are properly normalized, because Eq. (2) neglects the correlations between neighboring pixels introduced by image re-sampling. We considered accounting for these correlations; however, this would make the fitting code intolerably slow, as the resulting χ^2 would be non-diagonal. Using approximate errors in least squares (such as ignoring correlations) increases the actual variance of the estimators, but in the case considered here, the loss in photometric accuracy is below 1%. The real drawback of ignoring pixel correlations is that parameter uncertainties extracted from the fit are underestimated (since pixel correlations are positive); this is a product of any photometry method that assumes uncorrelated pixels on re-sampled or convolved images. Our geometric alignment technique, used to align images prior to the flux measurement as described in Sect. 3.2, uses a 3×3 pixel quadratic re-sampling kernel, which produces output pixels with an average variance of 80% of the input pixel variance, where the remaining 20% contributes to covariance in nearby pixels. We checked that flux variances (and covariances) computed assuming independent pixels are also underestimated by the same amount: on average, a 25% increase is required.

In order to derive accurate uncertainties, we used the fact that for each epoch, several images are available which measure the same object flux. Estimating fluxes on individual exposures rather than on stacks per night preserves the photometric precision since a common position is fit using all images. It also allows a check on the consistency of fluxes measured within a night. We therefore fit a common flux per night to the fluxes measured on each individual image by minimizing a χ_n^2 (where n stands for nights); this matrix is non-diagonal because the differential photometry produces correlated fluxes.

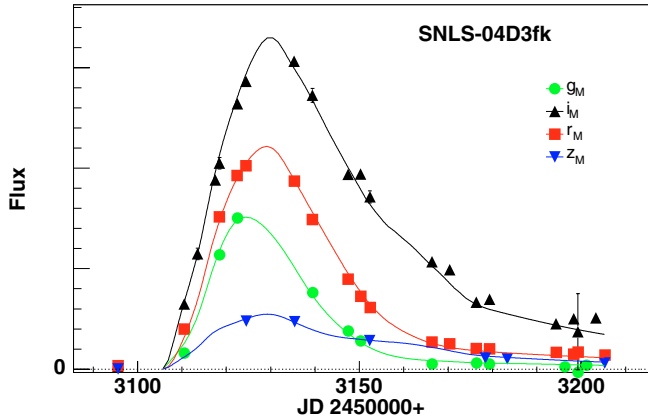


Fig. 1. Observed light-curves points of the SN Ia SNLS-04D3fk in g_M , r_M , i_M and z_M bands, along with the multi-color light-curve model (described in Sect. 5.1). Note the regular sampling of the observations both before and after maximum light. With a SN redshift of 0.358, the four measured pass-bands lie in the wavelength range of the light-curve model, defined by rest-frame U to R bands, and all light-curves points are therefore fitted simultaneously with only four free parameters (photometric normalization, date of maximum, a stretch and a color parameter).

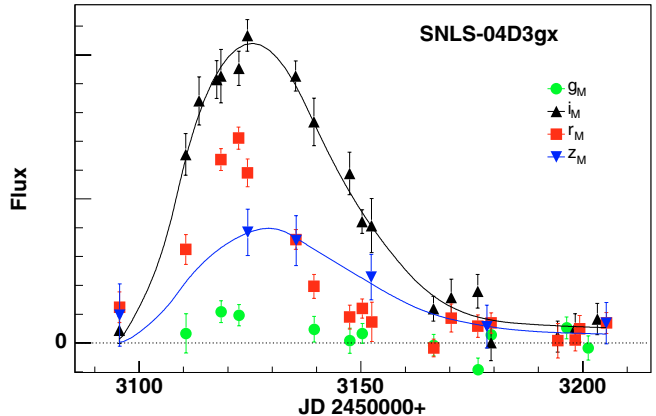


Fig. 2. Observed light-curves points of the SN Ia SNLS-04D3gx at $z = 0.91$. With a SN redshift of 0.91, only two of the measured pass-bands lie in the wavelength range of the light-curve model, defined by rest-frame U to R bands, and are therefore used in the fit (shown as solid lines). Note the excellent quality of the photometry at this high redshift value. Note also the clear signal observed in r_M and even in g_M , which correspond to central wavelength of respectively $\lambda \sim 3200 \text{ \AA}$ and $\lambda \sim 2500 \text{ \AA}$ in the SN rest-frame.

The χ_n^2 contribution of every individual image is evaluated, and outliers $>5\sigma$ (due to, for example, unidentified cosmic rays) are discarded; this cut eliminates 1.4% of the measurements on average. The covariance of the per-night fluxes is then extracted, and normalized so that the minimum χ_n^2 per degree of freedom is 1. This translates into an “effective” flux uncertainty derived from the scatter of repeated observations rather than from first principles. If the only source of noise (beyond photon statistics) were pixel correlations introduced by image resampling, we would expect an average $\chi_n^2/N_{\text{d.o.f.}}$ of 1.25, as all flux variances are on average under-estimated by 25%. Our average value is 1.55; hence we conclude that our photometric uncertainties are only $\sim 12\%$ ($\sqrt{(1.55/1.25)} - 1$) larger than photon statistics, leaving little margin for drastic improvement.

Table 2 summarizes the statistics of the differential photometry fits in each filter. The larger values of $\chi_n^2/N_{\text{d.o.f.}}$ in i_M and z_M probably indicate contributions from residual fringes. Examples of SNe Ia light-curves points are presented in Figs. 1 and 2 showing SNe at $z = 0.358$ and $z = 0.91$ respectively. Also shown on these figures are the results of the light-curves fits described in Sect. 5.1.

The next section discusses how accurately the SN fluxes can be extracted from the science frames relative to nearby field stars, i.e. how well the method assigns magnitudes to SNe, given magnitudes of the field stars which are used for photometric calibration, called tertiary standards hereafter.

3.4. Photometric alignment of supernovae relative to tertiary standards

The SN flux measurement technique of Sect. 3.2 delivers SN fluxes on the same photometric scale as the reference image. In this Section, we discuss how we measure ratios of the SN fluxes to those of the tertiary standards (namely stars in the

Table 2. Average number of images and nights per band for each SNLS light-curve. Note that there is less data in g_M and z_M . The χ_n^2 column refers to the last fit that imposes equal fluxes on a given night. The expected value is 1.25 (due to pixel correlations), so we face a moderate scatter excess of about 12% over photon statistics. The larger values in i_M and z_M indicate that fringes play a role in this excess. The last column displays the average wavelength of the effective filters in \AA .

Band	Average nb. of images	Average nb. of epochs	χ_n^2 per d.o.f.	Central wavelength
g_M	40	9.8	1.50	4860
r_M	75	14.4	1.40	6227
i_M	100	14.8	1.63	7618
z_M	60	7.9	1.70	8823

SNLS fields). The absolute flux calibration of the tertiary standards themselves is discussed in Sect. 4.

The image model that we use to measure the SN fluxes (Eq. (1)) can also be adapted to fit the tertiary standards by setting the “underlying galaxy model” to zero. We measure the fluxes of field stars by running the same simultaneous fit to the images used for the supernovae, but without the “zero-flux” images, and without an underlying galaxy. As this fitting technique matches that used for the SNe as closely as possible, most of the systematics involved (such as astrometric alignment residuals, PSF model uncertainties, and the convolution kernel modeling) cancel in the flux ratios.

For each tertiary standard (around 50 per CCD), we obtain one flux for each image (as done for the SNe), expressed in the same units. From the magnitudes of these fitted stars, we can extract a photometric zero point for the PSF photometry for every star on every image, which should be identical within measurement uncertainties. Several systematic checks were performed to search for trends in the fitted zero-points

as a function of several variables (including image number, star magnitude, and star color); no significant trends were detected. As zero-points are obtained from single measurements on single images, the individual measurements are both numerous and noisy, with a typical rms of 0.03 mag; however since they have the same expectation value, we averaged them using a robust fit to the distribution peak to obtain a single zero-point per observed filter.

To test how accurately the ratio of SN flux to tertiary standard stars is retrieved by our technique, we tested the method on simulated SNe. For each artificial supernova, we selected a random host galaxy, a neighboring bright star (the model star), and a down-scale ratio (r). For half of the images that enter the fit, we superimposed a scaled-down copy (by a factor r) of the model on the host galaxy. We rounded the artificial position at an integer pixel offset from the model star to avoid re-sampling. We then performed the full SN fit (i.e. one that allows for an underlying galaxy model and “zero flux images”) at the position of the artificial object, and performed the calibration star fit (i.e. one with no galaxy mode and no “zero-flux images”) at the original position of the model star. This matches exactly the technique used for the measurement and calibration of a real SN. We then compared the recovered flux ratio to the (known) down-scale ratio.

We found no significant bias as a function of SN flux or galaxy brightness at the level of 1%, except at signal-to-noise (S/N) ratios (integrated over the whole light-curve) below 10. At a S/N ratio of 10, fluxes are on average underestimated by less than 1%; this bias rises to about 3% at a S/N ratio of 7. This small flux bias disappears when the fitted object position is fixed, as expected because the fit is then linear. For this reason, when fitting z_M light-curves of objects at $z > 0.7$, for which the S/N is expected to be low, we use the fixed SN position from that obtained from the i_M and r_M fits.

Given the statistics of our simulations, the systematic uncertainty of SN fluxes due to the photometric method employed is less than 1% across the range of S/N we encounter in real data, and the observed scatter of the retrieved “fake SNe” fluxes behaves in the same way as that for real SNe. Over a limited range of S/N (more than 100 integrated over the whole light-curve), we can exclude biases at the 0.002 mag level. Our upper limits for a flux bias have a negligible impact on the cosmological conclusions drawn from the sample described here, and will likely be improved with further detailed simulations.

4. Photometric calibration

The supernova light-curves produced by the techniques described in Sect. 3.2 are calibrated relative to nearby field stars (the tertiary standards). Our next step is to place these instrumental fluxes onto a photometric calibration system using observations of stars of known magnitudes.

4.1. Photometric calibration of tertiary standards

Several standard star calibration catalogs are available in the literature, such as the Landolt (1983, 1992b) Johnson-Cousins (Vega-based) $UBVRI$ system, or the Smith et al. (2002)

$u'g'r'i'z'$ AB-magnitude system which is used to calibrate the Sloan Digital Sky Survey (SDSS). However, there are systematic errors affecting the transformations between the Smith et al. (2002) system and the widely used Landolt system. As discussed in Fukugita et al. (1996), these errors arise from various sources, for example uncertainties in the cross-calibration of the spectral energy distributions of the AB fundamental standard stars relative to that of Vega. Since the nearby SNe used in our cosmological fits were extracted from the literature and are typically calibrated using the standard star catalogs of Landolt (1992b), we adopted the same calibration source for our high-redshift sample. This avoids introducing additional systematic uncertainties between the distant and nearby SN fluxes, which are used to determine the cosmological parameters. To eliminate uncertainties associated with color corrections, we derive magnitudes in the natural MegaCam filter system.

Both standard and science fields were repeatedly observed over a period of about 18 months. Photometric nights were selected using the CFHT “Skyprobe” instrument (Cuillandre 2003), which monitors atmospheric transparency in the direction that the telescope is pointing. Only the 50% of nights with the smallest scatter in transparency were considered. For each night, stars were selected in the science fields and their aperture fluxes measured and corrected to an airmass of 1 using the average atmospheric extinction of Mauna Kea. These aperture fluxes were then averaged, allowing for photometric ratios between exposures. Stable observing conditions were indicated by a very small scatter in these photometric ratios (typically 0.2%); again the averaging was robust, with $5\text{-}\sigma$ deviations rejected. Observations of the Landolt standard star fields were processed in the same manner, though their fluxes were not averaged. The apertures were chosen sufficiently large (about $6''$ in diameter) to bring the variations of aperture corrections across the mosaic below 0.005 mag. However, since fluxes are measured in the same way and in the same apertures in science images and standard star fields, we did not apply any aperture correction.

Using standard star observations, we first determined zero-points by fitting linear color transformations and zero-points to each night and filter, however with color slopes common to all nights. In order to account for possible non-linearities in the Landolt to MegaCam color relations, the observed color-color relations were then compared to synthetic ones derived from spectrophotometric standards. This led to shifts of roughly 0.01 in all bands other than g_M , for which the shift was 0.03 due to the nontrivial relation to B and V .

We then applied the zero-points appropriate for each night to the catalog of science field stars of that same night. These magnitudes were averaged robustly, rejecting $5\text{-}\sigma$ outliers, and the average standard star observations were merged. Figure 3 shows the dispersion of the calibration residuals in the g_M , r_M , i_M and z_M bands. The observed standard deviation, which sets the upper bound to the repeatability of the photometric measurements, is about or below 0.01 mag in g_M , r_M and i_M , and about 0.016 mag in z_M .

For each of the four SNLS fields, a catalog of tertiary standards was produced using the procedure described above. These catalogs were then used to calibrate the supernova fluxes,

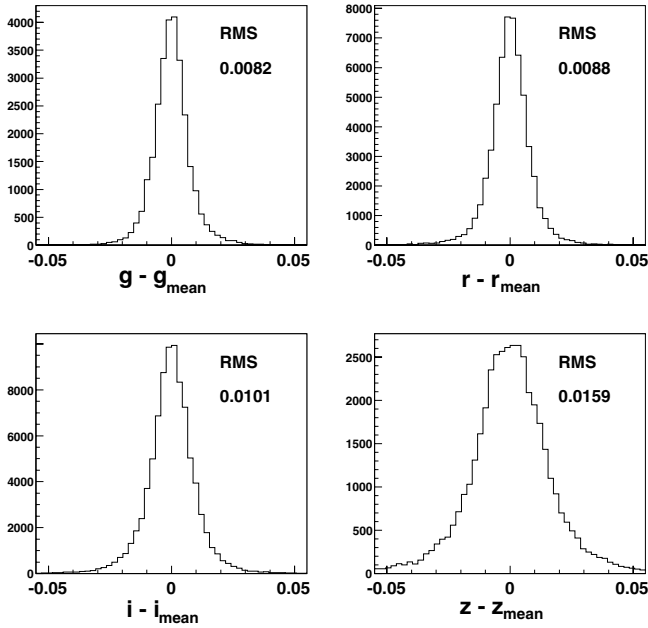


Fig. 3. The calibration residuals – i.e. the residuals around the mean magnitude of each Deep field tertiary standard – in the bands g_M , r_M , i_M and z_M , for all CCDs and fields, with one entry per star and epoch. The dispersion is below 1% in g_M , r_M and i_M , and about 1.5% in z_M .

as described in Sect. 3.4. The dominant uncertainty in the photometric scale of these catalogs comes from the determination of the color–color relations of the standard star measurements. For the g_M , r_M and i_M bands, a zero-point offset of 0.01 mag would easily be detected; hence we took this value as a conservative uncertainty estimate. The z_M band is affected by a larger measurement noise, and it is calibrated with respect to I and $R - I$ Landolt measurements. We therefore attributed to it a larger zero point uncertainty of 0.03 mag.

The MegaCam shutter is designed to preserve the mosaic illumination uniformity. Nevertheless, the shutter precision is a potential source of systematic uncertainties, given (1) the possible non uniformities due to the shutter motion and (2) the exposure time differences between the calibration images (a few seconds) and the science images (hundreds of seconds). For MegaCam, the *actual* exposure time is measured and reported for each exposure, using dedicated sensors. The shutter precision was investigated by Cuillandre (2005) and it was shown that the non-uniformity due to the shutter is less than 0.3% across the mosaic. Short and long exposures of the same fields were also compared. The systematic flux differences between the exposures were found to be below 1% (rms).

4.2. The MegaCam and Landolt instrumental filters

As the supernova fluxes are measured in the instrumental filter system, the MegaCam transmission functions (up to an arbitrary constant) are needed in order to correctly interpret the SN photometry. Similarly, for the published nearby supernovae which are reported in Landolt magnitudes, the filter responses of the Landolt system are required.

For the MegaCam filters, we used the measurements provided by the manufacturer, multiplied by the CCD quantum efficiency, the MegaPrime wide-field corrector transmission function, the CFHT primary mirror reflectivity, and the average atmospheric transmission at Mauna Kea. As an additional check, we computed synthetic MegaCam–SDSS color terms using the synthetic transmissions of the SDSS 2.5-m telescope (SDSS 2004b) and spectrophotometric standards taken from Pickles (1998) and Gunn & Stryker (1983). Since the SDSS science catalog (Finkbeiner et al. 2004; Raddick 2002; SDSS 2004a) shares thousands of objects with two of the four fields repeatedly observed with MegaCam, we were able to compare these synthetic color transformations with the observed transformations. We found a good agreement, with uncertainties at the 1% level. This constrains the central wavelengths of the MegaCam band passes to within 10 to 15 Å with respect to the SDSS 2.5m band passes.

The choice of filter band passes to use for Landolt-based observations is not unique. Most previous supernova cosmology works assumed that the determinations of Bessell (1990) describe the effective Landolt system well, although the author himself questions this fact, explicitly warning that the Landolt system “*is not a good match to the standard system*” – i.e. the historical Johnsons-Cousins system. Fortunately, Hamuy et al. (1992, 1994) provide spectrophotometric measurements of a few objects measured in Landolt (1992a); this enabled us to compare synthetic magnitudes computed using Bessell transmissions with Landolt measurements of the same objects. This comparison reveals small residual color terms which vanish if the B , V , R and I Bessell filters are blue-shifted by 41, 27, 21 and 25 Å respectively. Furthermore, if one were to assume that the Bessell filters describe the Landolt system, this would lead to synthetic MegaCam–Landolt color terms significantly different from the measured ones; the blue shifts determined above bring them into excellent agreement. We therefore assumed that the Landolt catalog magnitudes refer to blue-shifted Bessell filters, with a typical central wavelength uncertainty of 10 to 15 Å, corresponding roughly to a 0.01 accuracy for the color terms.

4.3. Converting magnitudes to fluxes

Given the variations with time of the cosmological scale factor $a(t)$, one can predict the evolution with redshift of the observed flux of classes of objects of reproducible luminosity though not necessarily known. This is why the cosmological conclusions that can be drawn from flux measurements rely on flux ratios of distant to nearby SNe, preferably measured in similar rest-frame pass-bands. The measured SNe magnitudes must therefore be converted to fluxes at some point in the analysis.

The flux in an imaginary rest-frame band of transmission T_{rest} for a SN at redshift z is deduced from the magnitude $m(T_{\text{obs}})$ measured in an observer band of transmission T_{obs} via:

$$f(z, T_{\text{rest}}) = 10^{-0.4(m(T_{\text{obs}}) - m_{\text{ref}}(T_{\text{obs}}))} \times \frac{\int \phi_{\text{SN}}(\lambda) T_{\text{rest}}(\lambda) d\lambda}{\int \phi_{\text{SN}}(\lambda) T_{\text{obs}}(\lambda(1+z)) d\lambda} \int \phi_{\text{ref}}(\lambda) T_{\text{obs}}(\lambda) d\lambda \quad (3)$$

where ϕ_{SN} is the spectrum of the SN, $m_{\text{ref}}(T)$ is the magnitude of some reference star that was used as a calibrator, and ϕ_{ref} is its spectrum. In this expression, the product of the first and third terms gives the integrated flux in the observed band, and the second term scales this integrated flux to the rest-frame band. We measure only $m(T_{\text{obs}}) - m_{\text{ref}}(T_{\text{obs}})$ (if the reference star is directly observed), or only $m(T_{\text{obs}})$ (if a non-observed star – e.g. Vega – is used as the reference). The reference spectrum, ϕ_{ref} , must be taken from the literature, as well as $m_{\text{ref}}(T_{\text{obs}})$ if the reference is not directly observed. The supernova spectrum, ϕ_{SN} , is taken to be a template spectrum appropriately warped to reproduce the observed color of the SN (as described in Guy et al. 2005). The quantity $f(z, T_{\text{rest}})$ scales as the inverse square of a luminosity distance:

$$\frac{f(z_1, T_{\text{rest}})}{f(z_2, T_{\text{rest}})} = \left(\frac{d_L(z_2)}{d_L(z_1)} \right)^2. \quad (4)$$

This conversion of a measured magnitude to a rest-frame flux (or a rest-frame magnitude) is usually integrated in the so-called cross-filter k-corrections (Kim et al. 1996; Nugent et al. 2002). In our case, it is integrated in the light-curve fit (Guy et al. 2005). (See Guy et al. (2005) for a discussion of the precise definitions of spectra and transmissions that enter into $f(z, T_{\text{rest}})$.)

Inspecting Eq. (3), we first note that the normalizations of T_{obs} and ϕ_{SN} cancel. The width of T_{obs} is a second order effect. When forming the ratio of two such quantities for two different SN, the normalization of ϕ_{ref} does not matter, nor the normalization of T_{rest} , provided the same T_{rest} is chosen for both objects. The width of T_{rest} matters only at the second order. The factors that do enter as first order effects are:

- $\int \phi_{\text{ref}}(\lambda) T_{\text{obs},1}(\lambda(1+z_1)) d\lambda / \int \phi_{\text{ref}}(\lambda) T_{\text{obs},2}(\lambda(1+z_2)) d\lambda$, which requires both the spectrum of a reference and the band passes of the observing systems, i.e. to first order, their central wavelengths,
- $m_{\text{ref}}(T_{\text{obs},1}) - m_{\text{ref}}(T_{\text{obs},2})$, i.e. the color of the reference. When comparing distant and nearby SNe, we typically rely on $B - R$ or $B - I$ colors,
- and obviously, the SNe measured magnitudes, or, more precisely, their difference.

We choose to use Vega as the reference star. An accurate spectrum of Vega was assembled by Hayes (1985). Some subtle differences are found by a more recent HST measurement (Bohlin & Gilliland 2004) but they only marginally affect broadband photometry: differences within the 1% uncertainty quoted in Hayes (1985) are found and we will assign this uncertainty to the Vega broadband fluxes. We use the HST-based measurement because it extends into the UV and NIR and hence is safe for the blue side of the U band and in the z_M band. For Vega, we adopt the magnitudes $(U, B, V, R_c, I_c) = (0.02, 0.03, 0.03, 0.03, 0.024)$ (Fukugita et al. (1996) and references therein). For other bands, a simple interpolation is adequate. Note that only Vega colors impact on cosmological measurements.

A possible shortcut consists in relying on spectrophotometric standards (Hamuy et al. 1992, 1994) which also have magnitudes on the Landolt system (Landolt 1992a). When we

compare synthetic Vega magnitudes of these objects with the photometric measurements, we find excellent matching of colors (at better than the 1% level), indicating that choosing Vega or spectrophotometric fluxes as the reference makes little practical difference.

4.4. Photometric calibration summary

We constructed catalogs of tertiary standard stars in the SNLS fields, expressed in MegaCam natural magnitudes, and defined on the Landolt standard system. The repeatability of measurements of a single star on a given epoch (including measurement noise) is about or below 0.01 mag rms in g_M , r_M and i_M , and about 0.016 mag in z_M . From standard star observations, we set conservative uncertainties of the overall scales of 0.01 mag in g_M , r_M and i_M and 0.03 in z_M . The MegaCam central wavelengths are constrained by color terms with respect to both the SDSS 2.5 m telescope and the Landolt catalog to within 10 to 15 Å. The central wavelengths of the band passes of the Landolt catalog are found slightly offset with respect to Bessell (1990), using spectrophotometric measurements of a subsample of this catalog.

5. Light-curve fit and cosmological analysis

To derive the brightness, light-curve shape and SN color estimates required for the cosmological analysis, the time sequence of photometric measurements for each SN was fit using a SN light-curve model. This procedure is discussed in this section together with the nearby and distant SN Ia samples selection and the cosmological analysis.

5.1. The SN Ia light-curve model

We fit the SN Ia light-curves in two or more bands using the SALT light-curve model (Guy et al. 2005) which returns the supernova rest-frame B -band magnitude m_B^* , a single shape parameter s and a single color parameter c . The supernova rest-frame B -band magnitude at the date of its maximum luminosity in B is defined as:

$$m_B^* = -2.5 \log_{10} \left(\frac{f(z, T_B^*, t = t_{\text{max},B})}{(1+z) \int \phi_{\text{ref}}(\lambda) T_B(\lambda) d\lambda} \right)$$

where $T_B^*(\lambda) \equiv T_B(\lambda/(1+z)) \equiv T_{\text{rest}}(B)$ is the rest-frame B -band transmission, and $f(z, T_B^*, t = t_{\text{max},B})$ is defined by Eq. (3). The stretch factor s is similar to that described in Perlmutter et al. (1997): it parameterizes the brighter-slower relation, originally described in Phillips (1993), by stretching the time axis of a unique light-curve template; $s = 1$ is defined in rest-frame B for the time interval -15 to $+35$ days using the Goldhaber et al. (2001) B -band template. For bands other than B , stretch is a parameter that indexes light-curve shape variability. The rest-frame color c is defined by $c = (B - V)_{B_{\text{max}}} + 0.057$: it is a color excess (or deficit) with respect to a fiducial SN Ia (for which $B - V = -0.057$ at B -band maximum light). Note that the color c is not just a measure of host galaxy extinction: c can accommodate both reddening by dust and any intrinsic color effect dependent or not on s . The reference value (-0.057) can be

changed without changing the cosmological conclusions, given the distance estimator we use (see Sect. 5.4).

The light-curve model was trained on very nearby supernovae (mostly at $z < 0.015$) published in the literature (see Guy et al. 2005 for the selection of these objects). Note that these training objects were *not* used in the Hubble diagram described in this paper. The SALT light-curve model generates light-curves in the observed bands at a given redshift, SALT also incorporates corrections for the Milky Way extinction, using the dust maps of Schlegel et al. (1998) coupled with the extinction law of Cardelli et al. (1989). The rest-frame coverage of SALT extends from 3460 to 6500 Å (i.e. slightly bluewards from U to R). We require that photometry is available in at least 2 measured bands with central wavelengths within this wavelength range to consider a SN for the cosmological analysis. Light curves in the z_M band become essential for $z > 0.80$, since at these redshifts, r_M corresponds to rest-frame $\lambda < 3460$ Å. All observed bands are fitted simultaneously, with common stretch and color parameters, global intensity and date of B -band maximum light. Making use of U -, B - and V -band measurements of nearby SNe Ia from the literature (mostly from Hamuy et al. 1996; Riess et al. 1999; Jha 2002), Guy et al. (2005) have constructed a distance estimator using either U - and B -band data or B - and V -band which shows a dispersion of 0.16 mag around the Hubble line. The fitted global intensity is then translated into a rest-frame- B observed magnitude at maximum light (m_B^*) which does not include any correction for brighter-slower or brighter-bluer relations.

The light-curve fit is carried out in two steps. The first fit uses all photometric data points to obtain a date of maximum light in the B -band. All points outside the range $[-15, +35]$ rest-frame days from maximum are then rejected, and the data refit. This restriction avoids the dangers of comparing light-curve parameters derived from data with different phase coverage: nearby SNe usually have photometric data after maximum light, but not always before maximum when the SN is rising, and almost never before -15 days. By contrast, SNLS objects have photometric sampling that is essentially independent of the phase of the light-curve because of the rolling-search observing mode, though late-time data (in the exponential tail) often has a poor S/N, or is absent due to field visibility.

5.2. The SN Ia samples

The cosmological analysis requires assembling a sample of nearby and distant SNe Ia.

We assembled a nearby SN Ia sample from the literature. Events with redshifts below $z = 0.015$ were rejected to limit the influence of peculiar velocities. We further retained only objects whose first photometric point was no more than 5 days after maximum light. To check for possible biases that this latter procedure might have introduced, we fitted subsets of data from objects with pre-maximum photometry. Our distance estimator (see Sect. 5.4) was found to be unaffected if the data started up to 7 days after maximum light. A sample of 44 nearby SNe Ia matched our requirements. Table 8 gives the SN name, redshift and filters used in the light-curve fits, as well as fitted

rest-frame B -band magnitude and values of the parameters s and c .

For this paper, we considered only distant SNe Ia that were discovered and followed during the first year of SNLS since this data set already constitutes the largest well controlled homogeneous sample of distant SN Ia. As discussed in Sect. 2.3, 91 objects were spectroscopically identified as “Ia” or “Ia*”, with a date of maximum light before July 15, 2004. Ten of these are not yet analyzed: 5 because images uncontaminated by SN light were not available at the time of this analysis, and 5 due to a limitation of our reduction pipeline which does not yet handle field regions observed with different CCDs. Six SNe have incomplete data due to either instrument failures, or persistent bad weather and two SNe, SNLS-03D3bb and SNLS-03D4cj, which happen to be spectroscopically peculiar (see Ellis et al., in prep.) have photometric data incompatible with the light-curve model.

The resulting fit parameters of the remaining 73 “Ia”+“Ia*” SNe are given in Table 9 and examples of light-curves measured in the four MegaCam bands are shown in Figs. 1 and 2, together with the result of the light-curve fit.

5.3. Host galaxy extinction

There is no consensus on how to correct for host galaxy extinction affecting high redshift SNe Ia. The pioneering SN cosmology papers (Riess et al. 1998; Perlmutter et al. 1999) typically observed in only one or two filters, and so had little or no color information with which to perform extinction corrections. Subsequent papers either selected low-extinction subsamples based on host galaxy diagnostics (Sullivan et al. 2003), or used multicolor information together with an assumed color of an unreddened SN to make extinction corrections on a subset of the data (Knop et al. 2003; Tonry et al. 2003).

These techniques have their drawbacks: the intrinsic color of SNe Ia has some dispersion, and measured colors often have large statistical errors in high-redshift data sets. When these two color uncertainties are multiplied by the ratio of total to selective absorption, $R_B \simeq 4$, the resulting error can be very large. To circumvent this, some studies used Bayesian priors (e.g. Riess et al. 1998; Tonry et al. 2003; Riess et al. 2004; Barris et al. 2004). Other authors argue that this biases the results (e.g. Perlmutter et al. 1999; Knop et al. 2003).

Here we employ a technique that makes use of color information to empirically improve distance estimates to SNe Ia. We exploit the fact that the SN color acts in the same direction as reddening due to dust – i.e. redder SNe are intrinsically dimmer, brighter SNe are intrinsically bluer (Tripp & Branch 1999). By treating the correction between color and brightness empirically, we avoid model-dependent assumptions that can both artificially inflate the errors and potentially lead to biases in the determination of cosmological parameters. Because we have more than one well-measured color for several SNe, we can perform consistency checks on this technique – distances from multiple colors should, and do, agree to a remarkable degree of precision (Sect. 6.3).

5.4. Cosmological fits

From the fits to the light-curves (Sect. 5.1), we computed a rest-frame- B magnitude, which, for perfect standard candles, should vary with redshift according to the luminosity distance. This rest-frame- B magnitude refers to *observed* brightness, and therefore does not account for brighter-slower and brighter-bluer correlations (see Guy et al. 2005 and references therein). As a distance estimator, we use:

$$\mu_B = m_B^* - M + \alpha(s - 1) - \beta c$$

where m_B^* , s and c are derived from the fit to the light curves, and α , β and the absolute magnitude M are parameters which are fitted by minimizing the residuals in the Hubble diagram. The cosmological fit is actually performed by minimizing:

$$\chi^2 = \sum_{\text{objects}} \frac{(\mu_B - 5 \log_{10}(d_L(\theta, z)/10 \text{ pc}))^2}{\sigma^2(\mu_B) + \sigma_{\text{int}}^2},$$

where θ stands for the cosmological parameters that define the fitted model (with the exception of H_0), d_L is the luminosity distance, and σ_{int} is the intrinsic dispersion of SN absolute magnitudes. We minimize with respect to θ , α , β and M . Since d_L scales as $1/H_0$, only M depends on H_0 . The definition of $\sigma^2(\mu_B)$, the measurement variance, requires some care. First, one has to account for the full covariance matrix of m_B^* , s and c from the light-curve fit. Second, $\sigma(\mu_B)$ depends on α and β ; minimizing with respect to them introduces a bias towards increasing errors in order to decrease the χ^2 , as originally noted in Tripp (1998). When minimizing, we therefore fix the values of α and β entering the uncertainty calculation and update them iteratively. $\sigma(\mu_B)$ also includes a peculiar velocity contribution of 300 km s^{-1} . σ_{int} is introduced to account for the ‘‘intrinsic dispersion’’ of SNe Ia. We perform a first fit with an initial value (typically 0.15 mag), and then calculate the σ_{int} required to obtain a reduced $\chi^2 = 1$. We then refit with this more accurate value. We fit 3 cosmologies to the data: a Λ cosmology (the parameters being Ω_M and Ω_Λ), a flat Λ cosmology (with a single parameter Ω_M), and a flat w cosmology, where w is the constant equation of state of dark energy (the parameters are Ω_M and w).

The Hubble diagram of SNLS SNe and nearby data is shown in Fig. 4, together with the best fit Λ cosmology for a flat Universe. Two events lie more than 3σ away from the Hubble diagram fit: SNLS-03D4au is 0.5 mag fainter than the best-fit and SNLS-03D4bc is 0.8 mag fainter. Although, keeping or removing these SNe from the fit has a minor effect on the final result, they were not kept in the final cosmology fits (since they obviously depart from the rest of the population) which therefore make use of 44 nearby objects and 71 SNLS objects.

The best-fitting values of α and β are $\alpha = 1.52 \pm 0.14$ and $\beta = 1.57 \pm 0.15$, comparable with previous works using similar distance estimators (see for example Tripp 1998). As discussed by several authors (see Guy et al. (2005) and references therein), the value of β does differ considerably from $R_B = 4$, the value expected if color were only affected by dust reddening. This discrepancy may be an indicator of intrinsic color variations in the SN sample (e.g. Nobili et al. 2003),

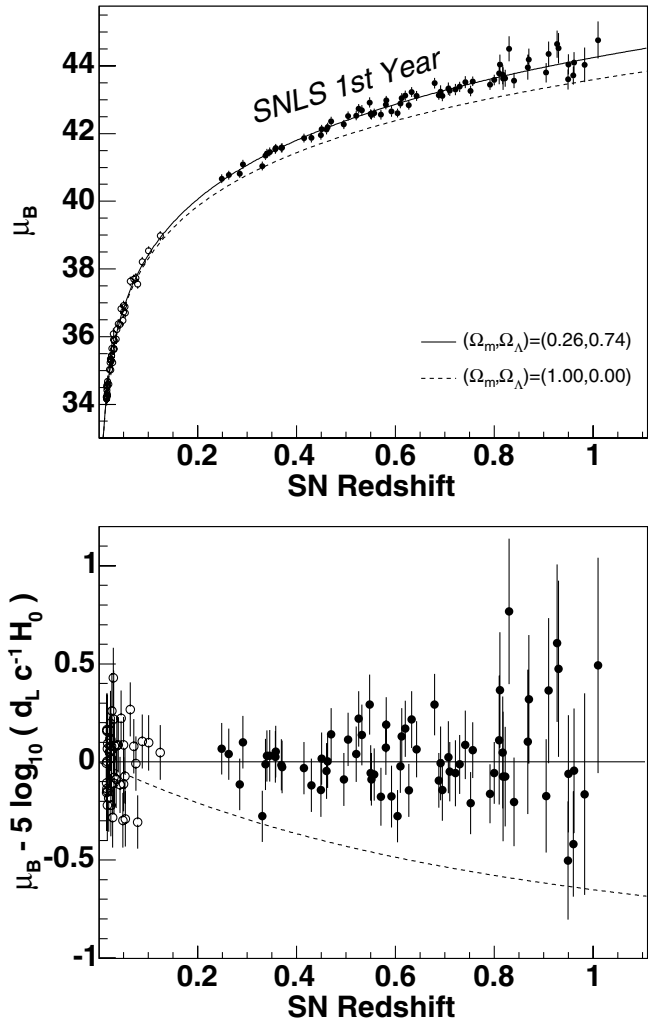


Fig. 4. Hubble diagram of SNLS and nearby SNe Ia, with various cosmologies superimposed. The bottom plot shows the residuals for the best fit to a flat Λ cosmology.

and/or variations in R_B . For the absolute magnitude M , we obtain $M = -19.31 \pm 0.03 + 5 \log_{10} h_{70}$.

The parameters α , β and M are nuisance parameters in the cosmological fit, and their uncertainties must be accounted for in the cosmological error analysis. The resulting confidence contours are shown in Figs. 5 and 6, together with the product of these confidence estimates with the probability distribution from baryon acoustic oscillations (BAO) measured in the SDSS (Eq. (4) in Eisenstein et al. 2005). We impose $w = -1$ for the $(\Omega_M, \Omega_\Lambda)$ contours, and $\Omega_k = 0$ for the (Ω_M, w) contours. Note that the constraints from BAO and SNe Ia are quite complementary. The best-fitting cosmologies are given in Table 3.

Using Monte Carlo realizations of our SN sample, we checked that our estimators of the cosmological parameters are unbiased (at the level of 0.1σ), and that the quoted uncertainties match the observed scatter. We also checked the field-to-field variation of the cosmological analysis. The four Ω_M values (one for each field, assuming $\Omega_k = 0$) are compatible at 37% confidence level. We also fitted separately the Ia and Ia* SNLS samples and found results compatible at the 75% confidence level.

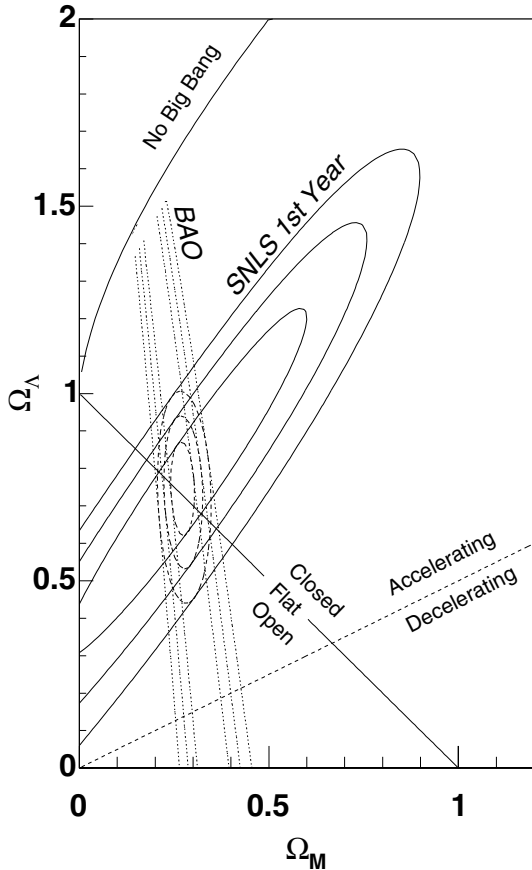


Fig. 5. Contours at 68.3%, 95.5% and 99.7% confidence levels for the fit to an $(\Omega_M, \Omega_\Lambda)$ cosmology from the SNLS Hubble diagram (solid contours), the SDSS baryon acoustic oscillations (Eisenstein et al. 2005, dotted lines), and the joint confidence contours (dashed lines).

Table 3. Cosmological parameters and statistical errors of Hubble diagram fits, with the BAO prior where applicable.

Fit	Parameters (stat only)
$(\Omega_M, \Omega_\Lambda)$	$(0.31 \pm 0.21, 0.80 \pm 0.31)$
$(\Omega_M - \Omega_\Lambda, \Omega_M + \Omega_\Lambda)$	$(-0.49 \pm 0.12, 1.11 \pm 0.52)$
$(\Omega_M, \Omega_\Lambda)$ flat	$\Omega_M = 0.263 \pm 0.037$
$(\Omega_M, \Omega_\Lambda) + \text{BAO}$	$(0.271 \pm 0.020, 0.751 \pm 0.082)$
$(\Omega_M, w) + \text{BAO}$	$(0.271 \pm 0.021, -1.023 \pm 0.087)$

We derive an intrinsic dispersion, $\sigma_{\text{int}} = 0.13 \pm 0.02$, appreciably smaller than previously measured (Riess et al. 1998; Perlmutter et al. 1999; Tonry et al. 2003; Barris et al. 2004; Riess et al. 2004). The intrinsic dispersions of nearby only (0.15 ± 0.02) and SNLS only (0.12 ± 0.02) events are statistically consistent although SNLS events show a bit less dispersion.

A notable feature of Fig. 4 is that the error bars increase significantly beyond $z = 0.8$, where the z_M photometry is needed to measure rest-frame $B - V$ colors. The z_M data is affected by a low signal-to-noise ratio because of low quantum efficiency and high sky background. For $z > 0.8$, $\sigma((B - V)_{\text{restframe}}) \approx 1.6\sigma(i_M - z_M)$, because the lever arm between the central wavelengths of i_M and z_M is about 1.6 times lower than for B and V .

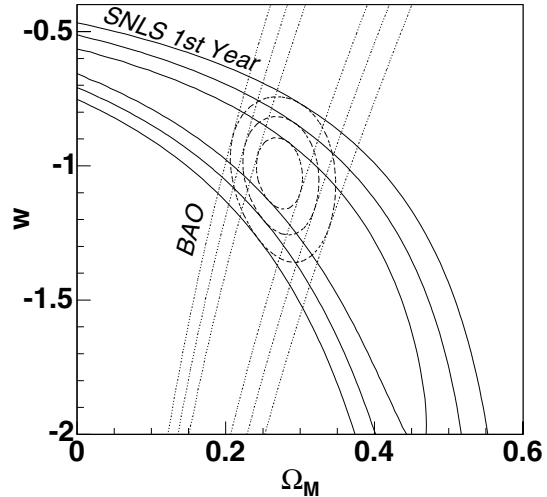


Fig. 6. Contours at 68.3%, 95.5% and 99.7% confidence levels for the fit to a flat (Ω_M, w) cosmology, from the SNLS Hubble diagram alone, from the SDSS baryon acoustic oscillations alone (Eisenstein et al. 2005), and the joint confidence contours.

Furthermore, errors in rest-frame color are scaled by a further factor of $\beta \approx 1.6$ in the distance modulus estimate. With a typical measurement uncertainty $\sigma(z_M) \approx 0.1$, we have a distance modulus uncertainty $\sigma(\mu) > 0.25$. Since the fall 2004 semester, we now acquire about three times more z_M data than for the data in the current paper, and this will improve the accuracy of future cosmological analyses.

The distance model we use is linear in stretch and color. Excluding events at $z > 0.8$, where the color uncertainty is larger than the natural color dispersion, we checked that adding quadratic terms in stretch or color to the distance estimator decreases the minimum χ^2 by less than 1. We hence conclude that the linear distance estimator accurately describes our sample.

Since the distance estimator we use depends on the color parameter c , residuals to the Hubble Diagram are statistically correlated to c . The correlation becomes very apparent when the c measurement uncertainty dominates the distance uncertainty budget, as happens in our sample when $z > 0.8$. We checked that the measurement uncertainties can account for the observed residual- c correlation at $z > 0.8$. Because of this correlation, color selected sub-samples mechanically lead to biased estimations of cosmological parameters.

6. Comparison of nearby and distant SN properties

6.1. Stretch and color distributions

The distributions of the shape and color parameters – s and c as defined in Sect. 5.1 – are compared in Figs. 7 and 8 for nearby objects and for SNLS supernovae at $z < 0.8$ for which c is accurately measured. These distributions look very similar, both in central value and shape. The average values for the two samples differ by about 1σ in stretch and 1.5σ in color: we find that distant supernovae are on average slightly bluer and slower than nearby ones. The statistical significance of the differences is low and the differences can easily be interpreted in terms of selection effects rather than evolution. The evolution of

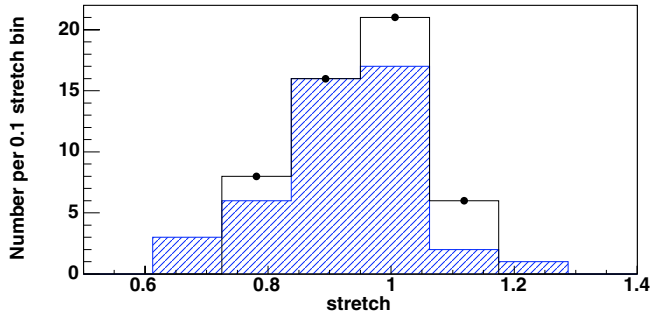


Fig. 7. The stretch (s parameter) distributions of nearby (hashed blue) and distant (thick black with filled symbols) SNLS SNe with $z < 0.8$. These distributions are very similar with averages of 0.920 ± 0.018 and 0.945 ± 0.013 , respectively (1σ apart).

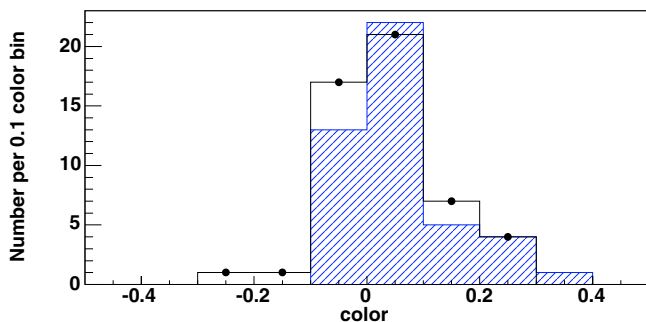


Fig. 8. The color (c parameter) distributions for nearby (hashed blue) and distant (thick black with filled symbols) SNLS SNe with $z < 0.8$. These distributions are very similar, with averages of 0.059 ± 0.014 and 0.029 ± 0.015 , respectively (1.5σ apart).

average s and c parameters with redshift is shown in Sect. 7.4; stretch is not monotonic, and color seems to drift towards the blue with increasing redshift. We show in Sect. 7.4 that the bulk of this effect can be reproduced by selection effects applied to an unevolving population.

6.2. Brighter-slower and brighter-bluer relationships

Figures 9 and 10 compare the nearby and distant samples in the stretch-magnitude and color-magnitude planes. There is no significant difference between these samples.

In Fig. 8, two of the SNLS events (SNLS-04D1ag and SNLS-04D3oe) have a color value, c , smaller than -0.1 . These supernovae are both classified as secure Ia. There are no SNe Ia in the nearby sample that are this blue. Figure 10 shows that these events lie on the derived brighter-bluer relation. Although they are brighter than average, fitting with or without these two events changes the cosmological results by less than 0.1σ .

6.3. Compatibility of SN colors

The measurement of distances to high redshift SNLS SNe involves the rest-frame U band. The MegaCam r_M band shifts from rest-frame B at $z = 0.5$ to rest-frame U at $z = 0.8$. Within this redshift range, distances are estimated mainly using i_M and r_M , the weight of z_M being affected by high photometric

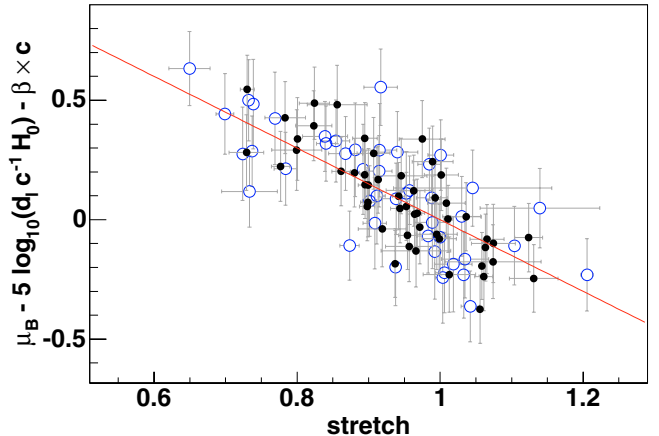


Fig. 9. Residuals in the Hubble diagram as a function of stretch (s parameter), for nearby (blue open symbols) and distant ($z < 0.8$, black filled symbols). This diagram computes distance modulus μ_B without the stretch term $\alpha(s - 1)$, and returns the well-known brighter-slower relationship with a consistent behavior for nearby and distant SNe Ia.

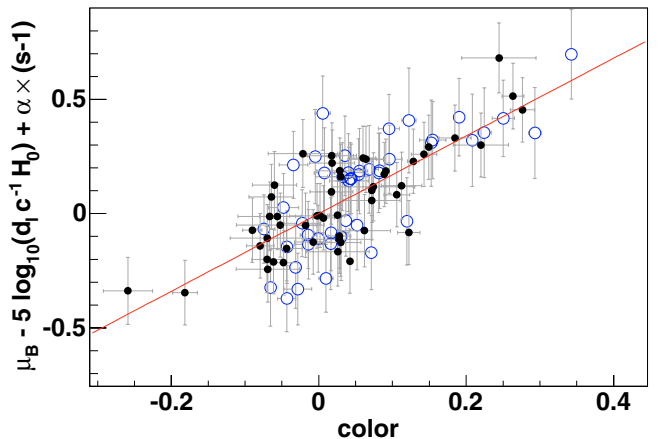


Fig. 10. Residuals in the Hubble diagram as a function of color (c parameter), for nearby (blue open symbols) and distant ($z < 0.8$, black filled symbols). This diagram computes distance modulus μ_B without the color term βc , and returns the brighter-bluer relationship with a consistent behavior for nearby and distant SNe Ia. Notice that the bluest SNLS objects are compatible with the bulk behavior.

noise; the (r_M, i_M) pair roughly changes from rest-frame (B, V) to rest-frame (U, B) .

Our cosmological conclusions rely on having a consistent distance estimate when using rest-frame BV and UB . This property is tested in Guy et al. (2005). However, it can be tested further on the subset of SNLS data having at least three usable photometric bands. The test proceeds as follows:

1. We fit the three bands at once, and store the stretch and date of maximum B light.
2. We fit the two reddest bands (BV for nearby objects), with the stretch, and date of maximum being fixed at the previously obtained values. From the fitted light-curve model we extract the expected rest-frame U band magnitude at maximum B light, U_{BV} .
3. We fit the two bluest bands, (UB for nearby objects), still with the stretch and date of maximum fixed. From this fit,

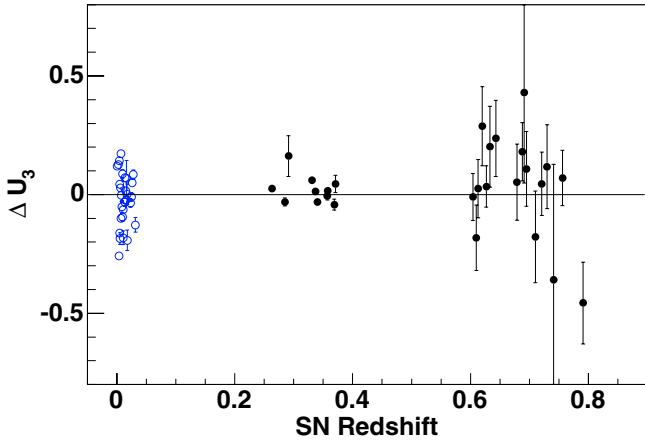


Fig. 11. ΔU_3 , difference between rest-frame U peak magnitude “predicted” from B and V , and the measured value, as a function of redshift. The error bars reflect photometric uncertainties. The redshift regions have been chosen so that the measured bands roughly sample the UBV rest-frame region. The differences between average values for the three samples agree within statistical uncertainties, indicating that the relation between U , B and V brightnesses does not change with redshift. Although the nearby and intermediate samples have comparable photometric resolution, the intermediate sample exhibits a far smaller scatter. We attribute this difference to the practical difficulties in calibrating U band observations.

we extract the expected rest-frame U band magnitude at maximum B light. Since it matches the measurement when the actual U flux is measured, we call it U_{meas} .

The test quantity is $\Delta U_3 \equiv U_{BV} - U_{\text{meas}}$, i.e. the “predicted” U (derived from B and V) minus the measured U brightness. Forcing both quantities to be measured with the same stretch and B maximum date is not essential, but narrows the distribution of residuals. A residual of zero means that the three measured bands agree with the light-curve model for a certain parameter set, and hence that the distance estimate will be identical for the two different color fits.

There are 10 SNLS “intermediate” redshift events at $0.25 < z < 0.4$, where $g_M r_M i_M$ sample the UBV rest-frame region, and 17 “distant” events at $0.55 < z < 0.8$, where UBV shifts to the $r_M i_M z_M$ triplet. We also have at our disposal a sample of 28 “nearby” objects measured in UBV , both from the nearby sample described in Table 8, and also from the light-curve model training sample which consists mainly of very nearby objects (see Guy et al. 2005). Figure 11 displays the value of ΔU_3 as a function of redshift and Table 4 summarizes the averages and dispersions. A very small scatter (about 0.033) is found for the intermediate redshift sample. The nearby and distant samples exhibit larger scatters; the nearby sample is probably affected by the practical difficulties in calibrating U observations, and our distant sample is affected by the poor S/N in the z_M band. We conclude from this study that our light curves model accurately describes the relations between the supernovae colors. Note that this ΔU_3 indicator is a promising tool for photometric classification of SNe Ia, provided its scatter remains comparable to that found for the intermediate redshift sample.

Table 4. Statistics of the 3 samples displayed in Fig. 11.

Sample	Bands	Events	rms	Average
nearby	UBV	28	0.122	0.0008 ± 0.023
intermediate	$g_M r_M i_M$	10	0.033	0.009 ± 0.010
high- z	$r_M i_M z_M$	17	0.156	0.039 ± 0.035

Table 5. Influence of a photometric calibration error on the cosmological parameters.

Band	Zero-point shift	$\delta\Omega_M$ (flat)	$\delta\Omega_{\text{tot}}$	δw (fixed Ω_M)
g_M	0.01	0.000	-0.02	0.00
r_M	0.01	0.009	0.03	0.02
i_M	0.01	-0.014	0.17	-0.04
z_M	0.03	0.018	-0.48	-0.03
sum	–	0.024	0.51	0.05

The same exercise can be done without imposing identical stretch and date of maximum light on the two fits. Rather than testing the light curves model, one then tests for potential biases in color estimates (leading to biases in distance estimates). The conclusions are the same as with fixed parameters: the samples have averages consistent with 0, and the dispersion of the central sample increases from 0.033 to 0.036.

7. Systematic uncertainties

We present, in this section, estimates of the systematic uncertainties possibly affecting our cosmological parameter measurements.

7.1. Photometric calibration and filter band-passes

We simulated a zero-point shift by varying the magnitudes of the light-curve points, one band at a time. Table 5 gives the resulting shifts in the derived cosmological parameters from the calibration errors derived in Sect. 4.1. We assume that errors in the $g_M r_M i_M z_M$ zero-points are independent, and propagate these 4 errors quadratically to obtain the total effect on cosmology.

We rely on the spectrum of one object, Vega (α Lyrae), to transform magnitudes into fluxes; the broadband flux errors for Vega are about 1% (Hayes (1985) and Sect. 4.3). To take into account the Vega flux and broadband color uncertainties, we simulated a flux error linear in wavelength that would offset the Vega ($B - R$) color by 0.01. The impact on Ω_M is ± 0.012 .

Uncertainties in the filter bandpasses affect the determination of supernovae brightnesses; the first-order effect is from errors in the central wavelengths. In the color–color relations (Landolt/MegaCam and SDSS/MegaCam – Sect. 4.2), we were able to detect shifts of 10 Å (corresponding roughly to a change of 0.01 in the color term). The effect of this shift is in fact very small: only the r_M filter has a sizable impact of ± 0.007 on Ω_M .

7.2. Light-curve fitting, $(U - B)$ color and k -corrections

If the light-curve model fails to properly describe the true light-curve shape, the result would be a bias in the light-curve parameters, and possibly in the cosmological parameters if the bias depends on redshift. We have already discussed two possible causes of such a bias: the influence of the first measurement date (Sect. 5.2), and the choice of rest-frame bands used to measure brightness and color (Sect. 6.3). Both have very small effects. However, given only 10 intermediate redshift SNLS events, each with an uncertainty of 0.033, the precision with which we can define the average $(U - B)$ color at given $(B - V)$ is limited to about 0.01 mag by our sample size.

Uncertainties in the k -corrections (due to SNe Ia spectral variability at fixed color) contribute directly to the observed scatter. The redshift range of the intermediate redshift sample of Sect. 6.3 corresponds to a rest-frame wavelength span of about 400 Å, in a region where SNe Ia spectra are highly structured. Since we observe compatible intrinsic dispersions for nearby and SNLS events (indeed, slightly lower for SNLS), we find no evidence that k -correction uncertainties add significantly to the intrinsic dispersion.

Nevertheless, since the measured scatter of the intermediate redshift sample appears surprisingly small and, since the sample size is small, we used a more conservative value of 0.02 for the light-curve model error, to account for both the errors in the colors and from k -corrections. A shift of the U -band light-curve model of 0.02 mag results in a change in Ω_M of 0.018. This is to be added to the statistical uncertainty.

7.3. U -band variability and evolution of SNe Ia

Concerns have been expressed regarding the use of rest-frame U -band fluxes to measure luminosity distances (e.g. Jha 2002 and Nugent et al. 2002), motivated by the apparent large variability of the U -band luminosity of SNe Ia. Such variability seems also to be present at intermediate redshifts although there seems to be little obvious evolution to $z = 0.5$ of the overall UV SED (Ellis et al., in prep.). Note that Guy et al. (2005) have succeeded in constructing a distance estimator using U - and B -band data which shows a dispersion of only 0.16 mag around the Hubble line, comparable to that found for distances derived using B - and V -band data. Note also that the quantity ΔU_3 appears to be independent of redshift, implying that if the average luminosity of SNe Ia evolves with redshift, this evolution must preserve the UBV rest-frame color relations. Lentz et al. (2000) predict a strong dependence of the UV flux from the progenitor metallicity (at fixed $B - V$ color), which should have been visible if metallicity evolution were indeed present.

7.4. Malmquist bias

The Malmquist bias may affect the cosmological conclusions by altering the average brightness of measured SNe in a redshift dependent way. The mechanism is however not exactly straightforward since the reconstructed distance depends on

stretch and color, and not only on the brightness. We have conducted simulations, both of nearby SN searches and of the SNLS survey, to investigate the effects on the derivation of cosmological parameters.

We simulated light-curves of nearby SNe Ia ($0.02 < z < 0.1$) with random explosion date, stretch and color, using the observed brighter-slower and brighter-bluer correlations. We then simulated a brightness cut at a fixed date. Although the number of “detected” events and their average redshift strongly depends on the brightness cut, the average distance bias of the survivors is found to change by less than 10%, when varying both the value and the sharpness of the brightness cut. The bias is also essentially independent of the discovery phase, although the peak brightness is not. We find a distance modulus bias of 0.027 (similar in B , V and R), sensitive at the 10% level to the unknown details of nearby searches. Note that the redshift dependence of the distance bias of the nearby sample has no impact on the cosmological measurements: only the average bias matters.

The crude simulation we conducted applies only to flux limited searches, which applies to about half of the sample. We compute an average bias value for our nearby sample as the simulation result (0.027 mag) times the fraction of events to which it applies. Assuming that both factors suffer from an uncertainty of 50%, we find an average nearby sample bias value of 0.017 ± 0.012 mag. A global increase of all nearby distances by $0.017(\pm 0.012)$ mag increases Ω_M (flat universe) by $0.019 (\pm 0.013)$.

For the distant SNLS sample, which is flux limited, we simulated supernovae at a rate per co-moving volume independent of redshift, accounted for the brighter-slower and brighter-bluer correlations, and adjusted the position and smoothness of the limiting magnitude cut in order to reproduce the redshift and peak magnitude distributions. In contrast with nearby SN simulations, here we have many observed distributions for a single search, and the key parameters that enter the simulation are highly constrained. The best match to SNLS data is shown in Fig. 12, and Fig. 13 shows the expected biases as a function of redshift in the shape and color parameters, and for our distance estimator. The distance modulus bias is about 0.02 mag at $z = 0.8$, increasing to 0.05 at $z = 1$. Correcting for the computed bias decreases Ω_M (flat Universe) by 0.02. We assumed that the uncertainty in this bias correction is 50% of its value.

To summarize: we find that the differential bias between nearby and distant samples almost exactly cancels, and estimate an overall uncertainty of 0.016 in Ω_M (flat Universe). Since applying the Malmquist bias corrections changes the cosmological results by less than 0.1σ , the corrections have not been applied. However, in the future, when the SNLS sample size increases, modeling and applying the Malmquist bias correction will assume a greater importance. The same applies to the nearby sample, where having a more controlled and homogeneous sample, discovered by a single search (e.g. SN Factory, Aldering et al. 2002) will be essential to reduce the associated systematic uncertainty.

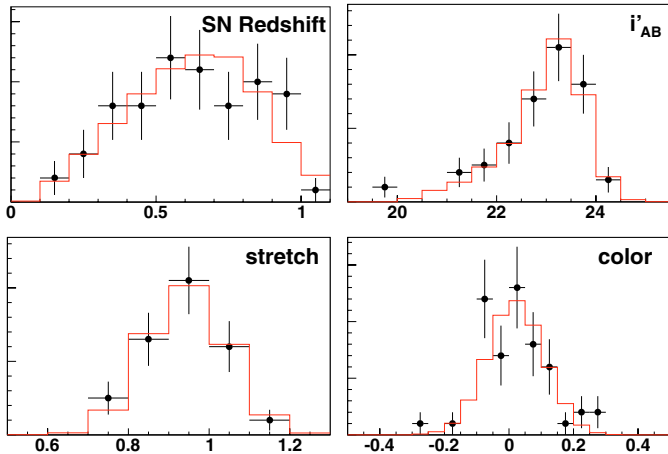


Fig. 12. Distributions of redshifts, peak i_M magnitudes (AB), stretch factors and colors of SNLS supernovae (black dots) together with the distributions obtained with simulated SNe (red histograms).

7.5. SNe Ib/c interlopers

All supernovae used here were spectroscopically identified as SN Ia, but we have labeled the least secure identifications as SN Ia* (Sect. 2.2, Howell et al. 2005). These 15 events are probable SN Ia but for this class a small amount of contamination by SNe Ib or SNe Ic (SNe Ib/c) is possible. We have checked that cosmological fits done with or without these events lead to the same cosmological conclusions (Sect. 5.4).

We also looked at estimating the SN Ib/c contamination in our sample. SNe Ib/c have an intrinsic luminosity distribution which is wider than SNe Ia (cf. dispersion 0.45 mag for SNe Ia, vs. 1.2 mag for SNe Ib/c; Homeier 2005; Richardson et al. 2002). After correcting for the SNe Ia brighter-slower and brighter-bluer correlations, a conservative estimate is that the SNe Ib/c scatter around the SNe Ia Hubble line with a dispersion 3 to 4 times larger than for SNe Ia. The first clue of SN Ib/c contamination would be the presence of objects with large residuals around the Hubble line; these contaminants should on average be fainter than SNe Ia at the same redshift. We have rejected two objects from the Hubble diagram (Sect. 5.4). Even if we consider both of these events to be SN Ib/c events, and assume that the dispersion of the SN Ia distribution about the Hubble line is 4 times smaller than for SNe Ib/c, we expect on average only 0.5 Ib/c interloper within the fitted sample.

For these reasons, we estimate the potential bias arising from the presence of non Ia events in our sample to be negligible.

7.6. Gravitational lensing and grey dust

Gravitational lensing by mass inhomogeneities may affect the apparent brightness of our supernovae. With respect to a uniform matter density, most of the events experience a tiny demagnification, and a small minority are amplified (see e.g. Holz & Wald 1998).

Whereas the average flux is conserved in the case of weak lensing, part of the SN light is lost when strong lensing produces multiple images among which some escape detection.

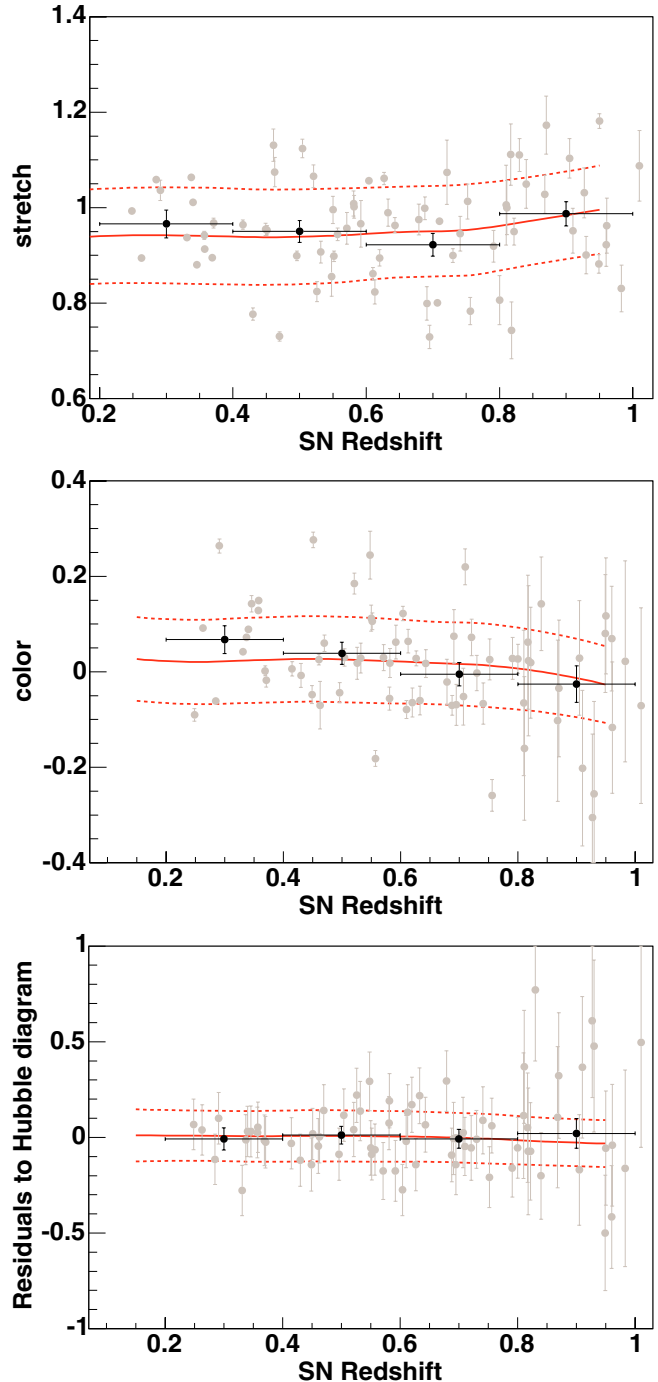


Fig. 13. Stretch, color and Hubble diagram residuals as a function of redshift for SNLS supernovae (gray dots). The black points correspond to average values in redshift bins. The red solid (dashed) lines represent the average (one standard deviation) values obtained with SNe simulations as described in Sect. 7.4. At large redshifts, since only bright SNe are identified, the average stretch factor is larger and the average color bluer. The average distance modulus is less affected by the selection (see text for details).

Multiple images of distant radio sources have been systematically searched by the CLASS survey (Myers et al. 2003) and have proved to be rare: the occurrence of multiple images separated by more than $0.3''$ and with flux ratio below 10:1 was found to be of 1 out of 690 with 1.44 secondary image on

average, with inefficiencies due to the separation and flux ratio cuts of 13% and 37% respectively (Browne et al. 2003). Multiple images with a smaller separation are not resolved in the SNLS, and their time delay is much smaller than the typical duration of a SN light curve² so that no flux is lost for such events. Hence CLASS results provide us with an upper limit for the number of (resolved) strong lensing cases in the SNLS supernova sample, given the fact that CLASS sources are globally more distant (see Chae 2003). Assuming (pessimistically) that for each strongly lensed SN, we see only one image, the flux bias is smaller than 0.3% at $z = 1$.

Gravitational lensing also broadens asymmetrically the brightness distribution of SNe at large redshifts (Bergström et al. 2000). As a consequence, a cosmological fit using SNe magnitudes (instead of fluxes) is biased. Holz & Linder (2004) found a dispersion of $0.088 \times z$ (note that Bergström et al. 2000 find a value of ~ 0.04 at $z = 1$ for smooth halo profiles in flat Λ CDM), which translates into a bias of the average magnitude of $\sim 0.004 \times z$. The broadening of the brightness distribution also affects the cosmological parameters uncertainties. In the cosmological fit, we have derived a constant “intrinsic” dispersion which includes the average dispersion due to lensing. Neglecting its redshift dependence has no significant impact on the accuracy of the errors derived for the cosmological parameters.

In summary, the total effect of lensing on cosmological parameters is very small. We find that Ω_M for a flat Λ CDM cosmology and the equation of state for a flat universe with BAO constraints, are shifted by at most -0.005 and -0.01 respectively. We therefore did not apply any correction to our results.

The possibility that SNe Ia could be dimmed by intergalactic grey dust (i.e. with weak extinction variation over the optical wavelengths) has been suggested by Aguirre (1999a,b) as an astrophysical alternative to the dark energy hypothesis. Some simple dust scenarios without a cosmological constant could be excluded by Riess et al. (2004) using SNe Ia data. Studying the colors of a large sample of quasars, Östman & Mörtzell (2005) were able to set limits on the light absorption length as a function of R_V , but these limits can only be translated into an upper bound of supernovae dimming. Conservatively assuming $R_V = 12$, using the SNOC program (Goobar et al. 2002), we computed an upper limit in the dimming of supernovae which translates into a shift of -0.025 in Ω_M for a Λ CDM cosmology, and a shift of -0.048 in w for a flat cosmology with constant equation of state when combined with SDSS BAO results. Note that these are upper limits and that a scenario without any intergalactic dust cannot be excluded. We therefore did not apply any correction to our results.

8. Summary and perspectives

Table 6 summarizes the uncertainties affecting our cosmological parameter measurements. The table includes the impact

² Delays are of order of a day for a source at $z = 1$ and a point-like lens at $z = 0.5$ for a typical angular separation of $0.2''$ (Bergström et al. 2000).

Table 6. Summary of uncertainties in the derived cosmological parameters. The dominant systematic uncertainty arises from the photometric calibration, itself dominated by the i_M and z_M band contributions.

Source	$\sigma(\Omega_M)$ (flat)	$\sigma(\Omega_{\text{tot}})$	$\sigma(w)$	$\sigma(\Omega_M)$ (with BAO)	$\sigma(w)$
Zero-points	0.024	0.51	0.05	0.004	0.040
Vega spectrum	0.012	0.02	0.03	0.003	0.024
Filter bandpasses	0.007	0.01	0.02	0.002	0.013
Malmquist bias	0.016	0.22	0.03	0.004	0.025
Sum (<i>sys</i>)	0.032	0.55	0.07	0.007	0.054
Meas. errors	0.037	0.52	0.09	0.020	0.087
$U - B$ color (<i>stat</i>)	0.020	0.10	0.05	0.003	0.021
Sum (<i>stat</i>)	0.042	0.53	0.10	0.021	0.090

of uncertainties in several parameter directions: the Ω_M direction for a flat (Ω_M, Ω_Λ) (i.e. $w = -1$) cosmology, the Ω_{tot} direction for a general (Ω_M, Ω_Λ) cosmology, and the w direction at fixed Ω_M for a (Ω_M, w) cosmology. We also report here the observed shifts when the BAO prior is applied to a flat (Ω_M, w) cosmology. Note that measurement and isolation of systematic errors is a major goal of the SNLS. Some of these uncertainties will decrease as more data is acquired and future papers will examine a wider range of issues, using our growing dataset.

Combining Tables 3 and 6, we obtain the following results:

$$\Omega_M = 0.263 \pm 0.042 \text{ (stat)} \pm 0.032 \text{ (syst)}$$

for a flat Λ cosmology, and

$$\Omega_M = 0.271 \pm 0.021 \text{ (stat)} \pm 0.007 \text{ (syst)}$$

$$w = -1.023 \pm 0.090 \text{ (stat)} \pm 0.054 \text{ (syst)}$$

$$w < -0.85 \text{ (95\% CL)}$$

for a flat cosmology with constant equation of state, when our constraints are combined with the BAO SDSS results. Assuming $w > -1$ brings our upper limit to -0.83 (at 95% CL). Supernovae alone give a marginal constraint: $w < -0.5$ at 95% CL.

These results agree well with previous works, both from SNe Ia, and also from other sources. For example Seljak et al. (2005) finds very similar results combining CMB, LSS and $\text{Ly}\alpha$ constraints. The dominant systematic uncertainties arise from the nearby sample and from the photometric calibration of the z_M band; both will be improved in the future. The multi-band light-curves allow us to study color relations as a function of redshift; these data are expected to be sensitive indicators of evolution. We observed a surprisingly narrow correlation between $(U - B)$ and $(B - V)$ (using the ΔU_3 indicator), indicating that the dispersion in U -band properties is well correlated with measurements in redder bands.

From the first year of SNLS data, we placed 71 distant events on the Hubble Diagram, with 10 more from the same period to be added later. (Our full first year statistics would have been around 100 SNe Ia with spectroscopic confirmation had we not lost Feb. 2004 to an instrument failure.) Our

time sampling, filter coverage, and image quality have now significantly improved since early 2004, and we now regularly acquire 2–3 times as much data in z_M . A precise photometric calibration is essential, and we are now working with the CFHTLS community in refining the photometric calibration of the MegaCam instrument. We have embarked on the process of calibrating tertiary standards in our fields, from Sloan secondary and primary standards. This will allow us to cross-check the Vega/Landolt zero-points, and more accurately calibrate z_M band observations.

After only two years of operation, the SNLS has already demonstrated its advantages over all previous ground-based supernova surveys. The “rolling search” technique is robust to weather and instrument-related problems, and the technical characteristics of the survey are now well understood. The average rate of spectroscopically-confirmed SNe Ia is currently about 10 per lunation and continues to increase. Up until July 2005, the SNLS sample includes more than 200 spectroscopically identified SNe Ia, most with excellent photometric temporal and filter coverage. An extrapolation of the current rate to the end of the survey indicates that we should reach our goal of building a Hubble diagram with about 700 spectroscopically identified well-measured SN Ia events. The SNLS already has the largest-ever sample of high- z SNe discovered by a single telescope, and will eventually produce a homogeneous, high-quality sample that is an order of magnitude larger still.

High statistical accuracy benefits the control of systematics. With our unmatched SN statistics, by year 5 we will be able to populate each ~ 0.1 redshift bin with ~ 100 SNe Ia, thus filling the brightness, decline-rate, and color 3-dimensional parameter space. This will enable us to detect possible drifts in “SNe Ia demographics”, and control Malmquist bias. Moreover, the rolling-search observing mode produces many events at low to intermediate redshift with superb photometric accuracy, because integration times are tailored for the faintest objects. These relatively bright events permit demanding internal consistency tests, and may lead to improvements in distance estimation.

Acknowledgements. The authors wish to recognize and acknowledge the very significant cultural role and reverence that the summit of Mauna Kea has always had within the indigenous Hawaiian community. We are most fortunate to have the opportunity to conduct observations from this mountain. We gratefully acknowledge the assistance of the CFHT Queued Service Observing Team, led by P. Martin (CFHT). We heavily rely on the dedication of the CFHT staff and particularly J.-C. Cuillandre for continuous improvement of the instrument performance. The real-time pipelines for supernovae detection run on computers integrated in the CFHT computing system, and are very efficiently installed, maintained and monitored by K. Withington (CFHT). We also heavily rely on the real-time Elixir pipeline which is operated and monitored by J.-C. Cuillandre, E. Magnier and K. Withington. We are grateful to L. Simard (CADC) for setting up the image delivery system and his kind and efficient responses to our suggestions for improvements. The French collaboration members carry out the data reductions using the CCIN2P3. Canadian collaboration members acknowledge support from NSERC and CIAR; French collaboration members from CNRS/IN2P3, CNRS/INSU, PNC and CEA. This work

was supported in part by the Director, Office of Science, Office of High Energy and Nuclear Physics, of the US Department of Energy. The France-Berkeley Fund provided additional collaboration support. CENTRA members were supported by Fundação para a Ciência e Tecnologia (FCT), Portugal under POCTI/FNU/43423. S. Fabbro and C. Gonçalves acknowledge support from FCT under grants no SFRH/BPD/14682/2003 and SFRH/BPD/11641/2002 respectively.

References

- Aguirre, A. 1999a, *ApJ*, 525, 583
 Aguirre, A. N. 1999b, *ApJ*, 512, L19
 Alard, C. 2000, *A&AS*, 144, 363
 Alard, C., & Lupton, R. H. 1998, *ApJ*, 503, 325
 Aldering, G., Adam, G., Antilogus, P., et al. 2002, in *Survey and Other Telescope Technologies and Discoveries*, ed. T. J. Anthony, & W. Sidney, *Proc. SPIE*, 4836, 61
 Altavilla, G., et al. 2004, *MNRAS*, 349, 1344
 Barris, B. J., Tonry, J. L., Blondin, S., et al. 2004, *ApJ*, 602, 571
 Basa, S., Astier, P., & Aubourg, E. 2005, in preparation
 Bergström, L., Goliath, M., Goobar, A., & Mörtzell, E. 2000, *A&A*, 358, 13
 Bertin, E., & Arnouts, S. 1996, *A&AS*, 117, 393
 Bessell, M. S. 1990, *PASP*, 102, 1181
 Bohlin, R. C., & Gilliland, R. L. 2004, *AJ*, 127, 3508
 Boulade, O., Charlot, X., Abbon, P., et al. 2003, in *Instrument Design and Performance for Optical/Infrared Ground-based Telescopes*, ed. Iye, Masanori; Moorwood, Alan F. M., *Proc. SPIE*, 4841, 72
 Browne, I. W. A., Wilkinson, P. N., Jackson, N. J. F., et al. 2003, *MNRAS*, 341, 13
 Cardelli, J. A., Clayton, G. C., & Mathis, J. S. 1989, *APJ*, 345, 245
 CFHTLS. 2002, http://cfht.hawaii.edu/Science/CFHTLS_Tech_rep.
 Chae, K.-H. 2003, *MNRAS*, 346, 746
 Cuillandre, J.-C. 2003, *SkyProbe at CFHT: Atmospheric Attenuation*, <http://www.cfht.hawaii.edu/Instruments/Elixir/skyprobe/>
 Cuillandre, J.-C. 2005, *Shutter ballistics and exposure time*, <http://cfht.hawaii.edu/Instruments/Imaging/MegaPrime>
 Eisenstein, D. J., Zehavi, I., Hogg, D. W., et al. 2005, *ApJ*, 633, 560
 Ellis, R., Sullivan, M., & Howell, D. 2005, in preparation
 Fabbro, S. 2001, Ph.D. Thesis, Université Denis Diderot, Paris
 Finkbeiner, D. P., Padmanabhan, N., Schlegel, D. J., et al. 2004, *AJ*, 128, 2577
 Fukugita, M., Ichikawa, T., Gunn, J. E., et al. 1996, *AJ*, 111, 1748
 Goldhaber, G., Groom, D. E., Kim, A., et al. 2001, *ApJ*, 558, 359
 Goobar, A., Mörtzell, E., Amanullah, R., et al. 2002, *A&A*, 392, 757
 Gunn, J. E., & Stryker, L. L. 1983, *ApJS*, 52, 121
 Guy, J., Astier, P., Nobili, S., Regnault, N., & Pain, R. 2005, *A&A*, 443, 781
 Hamuy, M., Phillips, M. M., Suntzeff, N. B., et al. 1996, *AJ*, 112, 2408
 Hamuy, M., Suntzeff, N. B., Heathcote, S. R., et al. 1994, *PASP*, 106, 566
 Hamuy, M., Walker, A. R., Suntzeff, N. B., et al. 1992, *PASP*, 104, 533
 Hayes, D. S. 1985, in *Calibration of Fundamental Stellar Quantities*, *IAU Symp.*, 111, 225
 Holz, D. E., & Linder, E. V. 2004 [[arXiv:astro-ph/0412173](http://arxiv.org/abs/astro-ph/0412173)]
 Holz, D. E., & Wald, R. M. 1998, *Phys. Rev. D*, 58, 063501
 Homeier, N. L. 2005, *ApJ*, 620, 12
 Howell, D. A., Sullivan, M., Perret, K., et al. 2005, *ApJ*, in press
 Jha, S. 2002, Ph.D. Thesis, University of Washington

- Kim, A., Goobar, A., & Perlmutter, S. 1996, *PASP*, 108, 190
- Knop, R. A., Aldering, G., Amanullah, R., et al. 2003, *ApJ*, 598, 102
- Krisciunas, K., Phillips, M. M., Stubbs, C., et al. 2001, *AJ*, 122, 1616
- Krisciunas, K., Phillips, M. M., Suntzeff, N. B., et al. 2004a, *AJ*, 127, 1664
- Krisciunas, K., Suntzeff, N. B., Phillips, M. M., et al. 2004b, *AJ*, 128, 3034
- Landolt, A. U. 1983, *AJ*, 88, 439
- Landolt, A. U. 1992a, *AJ*, 104, 372
- Landolt, A. U. 1992b, *AJ*, 104, 340
- Lentz, E. J., Baron, E., Branch, D., Hauschildt, P. H., & Nugent, P. E. 2000, *ApJ*, 530, 966
- Magnier, E. A., & Cuillandre, J.-C. 2004, *PASP*, 116, 449
- Myers, S. T., Jackson, N. J., Browne, I. W. A., et al. 2003, *MNRAS*, 341, 1
- Nobili, S., Goobar, A., Knop, R., & Nugent, P. 2003, *A&A*, 404, 901
- Nugent, P., Kim, A., & Perlmutter, S. 2002, *PASP*, 114, 803
- Östman, L., & Mörtzell, E. 2005, *JCAP*, 0502, 005
- Perlmutter, S., Gabi, S., Goldhaber, G., et al. 1997, *ApJ*, 483, 565
- Perlmutter, S., Aldering, G., Goldhaber, G., et al. 1999, *ApJ*, 517, 565
- Phillips, M. M. 1993, *ApJ*, 413, L105
- Pickles, A. J. 1998, *pas*, 110, 863
- Raddick, M. J. 2002, *BAAS*, 34, 1150
- Richardson, D., Branch, D., Casebeer, D., et al. 2002, *AJ*, 123, 745
- Riess, A. G., Filippenko, A. V., Challis, P., et al. 1998, *AJ*, 116, 1009
- Riess, A. G., Kirshner, R. P., Schmidt, B. P., et al. 1999, *AJ*, 117, 707
- Riess, A. G., Strolger, L., Tonry, J., et al. 2004, *ApJ*, 607, 665
- Schlegel, D. J., Finkbeiner, D. P., & Davis, M. 1998, *ApJ*, 500, 525
- SDSS 2004a, Sky Server, SDSS Data Release 3, <http://cas.sdss.org/dr3/en/>
- SDSS 2004b, Sky Server, SDSS Data Release 3, Imaging camera parameters and description, <http://www.sdss.org/dr3/instruments/imager/>
- Seljak, U., Makarov, A., McDonald, P., et al. 2005, *Phys. Rev. D*, 71, 103515
- Smith, J. A., Tucker, D. L., Kent, S., et al. 2002, *AJ*, 123, 2121
- Stetson, P. B. 1987, *PASP*, 99, 191
- Strolger, L.-G., Smith, R. C., Suntzeff, N. B., et al. 2002, *AJ*, 124, 2905
- Sullivan, M., Ellis, R. S., Aldering, G., et al. 2003, *MNRAS*, 340, 1057
- Sullivan, M., Howell, A., Perrett, K., et al. 2005, *AJ*, in press
- Tonry, J. L., Schmidt, B. P., Barris, B., et al. 2003, *ApJ*, 594, 1
- Tripp, R. 1998, *A&A*, 331, 815
- Tripp, R., & Branch, D. 1999, *ApJ*, 525, 209
- van Dokkum, P. G. 2001, *PASP*, 113, 1420
-
- ¹ LPNHE, CNRS-IN2P3 and Universités Paris VI & VII, 4 place Jussieu, 75252 Paris Cedex 05, France; e-mail: astier@in2p3.fr
- ² APC, Collège de France, 11 place Marcellin Berthelot, 75005 Paris, France
- ³ DSM/DAPNIA, CEA/Saclay, 91191 Gif-sur-Yvette Cedex, France
- ⁴ Department of Physics and Astronomy, University of Victoria, PO Box 3055, Victoria, BC V8W 3P6, Canada
- ⁵ LAM, CNRS, BP8, Traverse du Siphon, 13376 Marseille Cedex 12, France
- ⁶ Department of Astronomy and Astrophysics, University of Toronto, 60 St. George Street, Toronto, ON M5S 3H8, Canada
- ⁷ CENTRA-Centro M. de Astrofísica and Department of Physics, IST, Lisbon, Portugal
- ⁸ CPPM, CNRS-IN2P3 and Université Aix-Marseille II, Case 907, 13288 Marseille Cedex 9, France
- ⁹ University of Oxford Astrophysics, Denys Wilkinson Building, Keble Road, Oxford OX1 3RH, UK
- ¹⁰ Université de Savoie, 73000 Chambéry, France
- ¹¹ LBNL, 1 Cyclotron Rd, Berkeley, CA 94720, USA
- ¹² ESO, Alonso de Cordova 3107, Vitacura, Casilla 19001, Santiago 19, Chile
- ¹³ CRAL, 9 avenue Charles André, 69561 Saint-Genis-Laval cedex, France
- ¹⁴ California Institute of Technology, Pasadena, California, USA
- ¹⁵ LUTH, UMR 8102, CNRS and Observatoire de Paris, 92195 Meudon, France
- ¹⁶ Department of Physics, Stockholm University, Sweden
- ¹⁷ IoA, University of Cambridge, Madingley Road, Cambridge CB3 0EZ, UK
- ¹⁸ Department of Physics, University of California Berkeley, Berkeley, CA 94720, USA

Online Material

Table 7. Transients from the first year sample identified as SNIa or SNIa*.

Name	RA(2000)	Dec(2000)	Obs. date ^a	Tel./Inst. ^b	Spectral type ^c	z^d	z source
SNLS-03D1au	02:24:10.392	-04:02:14.93	2907	Keck/LRIS	SNIa	0.504	gal
SNLS-03D1aw	02:24:14.786	-04:31:01.61	2907	Keck/LRIS	SNIa	0.582	gal
SNLS-03D1ax	02:24:23.338	-04:43:14.28	2913	Gem/GMOS	SNIa	0.496	gal
SNLS-03D1bf	02:24:02.375	-04:55:57.27	2909	VLT/FORS1	SNIa*	0.703	gal
SNLS-03D1bk	02:26:27.412	-04:32:11.95	2912	Gem/GMOS	SNIa	0.865	gal
SNLS-03D1bp	02:26:37.714	-04:50:19.55	2910	VLT/FORS1	SNIa*	0.346	gal
SNLS-03D1cm	02:24:55.294	-04:23:03.61	2940	Gem/GMOS	SNIa	0.87	SN
SNLS-03D1co	02:26:16.252	-04:56:05.65	2966	Keck/LRIS	SNIa	0.679	gal
SNLS-03D1dj	02:26:19.087	-04:07:08.89	2964	Keck/LRIS	SNIa	0.39	SN
SNLS-03D1dt	02:26:31.200	-04:03:08.51	2974	VLT/FORS1	SNIa	0.612	gal
SNLS-03D1ew	02:24:14.079	-04:39:56.93	2995	Gem/GMOS	SNIa	0.868	gal
SNLS-03D1fb	02:27:12.875	-04:07:16.44	2641	VLT/FORS1	SNIa	0.498	gal
SNLS-03D1fc	02:25:43.625	-04:08:38.93	2641	VLT/FORS1	SNIa	0.331	gal
SNLS-03D1fl	02:25:58.329	-04:07:44.17	2641	VLT/FORS1	SNIa	0.688	gal
SNLS-03D1fq	02:26:55.683	-04:18:08.10	2998	Gem/GMOS	SNIa	0.80	SN
SNLS-03D1gt	02:24:56.027	-04:07:37.11	2641	VLT/FORS1	SNIa	0.55	SN
SNLS-03D3af	14:21:14.955	+52:32:15.68	2737	Keck/LRIS	SNIa	0.532	gal
SNLS-03D3aw	14:20:53.534	+52:36:21.04	2767	Keck/LRIS	SNIa	0.449	gal
SNLS-03D3ay	14:17:58.448	+52:28:57.63	2766	Keck/LRIS	SNIa	0.371	gal
SNLS-03D3ba	14:16:33.465	+52:20:32.02	2766	Keck/LRIS	SNIa	0.291	gal
SNLS-03D3bb	14:16:18.920	+52:14:53.66	2766	Keck/LRIS	SNIa	0.244	gal
SNLS-03D3bh	14:21:35.894	+52:31:37.86	2766	Keck/LRIS	SNIa	0.249	gal
SNLS-03D3bl	14:19:55.844	+53:05:50.91	2792	Keck/LRIS	SNIa	0.355	gal
SNLS-03D3cc	14:19:45.192	+52:32:25.76	2793	Keck/LRIS	SNIa	0.463	gal
SNLS-03D3cd	14:18:39.963	+52:36:44.22	2792	Keck/LRIS	SNIa	0.461	gal
SNLS-03D4ag	22:14:45.806	-17:44:22.95	2824	Keck/LRIS	SNIa	0.285	gal
SNLS-03D4at	22:14:24.023	-17:46:36.03	2826	VLT/FORS1	SNIa	0.633	gal
SNLS-03D4au	22:16:09.917	-18:04:39.19	2826	VLT/FORS1	SNIa*	0.468	gal
SNLS-03D4bc	22:15:28.143	-17:49:48.66	2826	VLT/FORS1	SNIa	0.572	gal
SNLS-03D4cj	22:16:06.658	-17:42:16.83	2879	Keck/LRIS	SNIa	0.27	SN
SNLS-03D4cn	22:16:34.600	-17:16:13.55	2879	Gem/GMOS	SNIa	0.818	gal
SNLS-03D4cx	22:14:33.754	-17:35:15.35	2885	VLT/FORS1	SNIa	0.95	SN
SNLS-03D4cy	22:13:40.441	-17:40:54.12	2909	Gem/GMOS	SNIa	0.927	gal
SNLS-03D4cz	22:16:41.845	-17:55:34.40	2910	Gem/GMOS	SNIa	0.695	gal
SNLS-03D4dh	22:17:31.040	-17:37:46.98	2906	Keck/LRIS	SNIa	0.627	gal
SNLS-03D4di	22:14:10.249	-17:30:24.18	2885	VLT/FORS1	SNIa	0.905	gal
SNLS-03D4dy	22:14:50.513	-17:57:23.24	2912	VLT/FORS1	SNIa	0.60	SN
SNLS-03D4fd	22:16:14.462	-17:23:44.33	2937	Gem/GMOS	SNIa	0.791	gal
SNLS-03D4gf	22:14:22.907	-17:44:02.49	2641	VLT/FORS1	SNIa*	0.58	SN
SNLS-03D4gg	22:16:40.185	-18:09:51.82	2641	VLT/FORS1	SNIa	0.592	gal
SNLS-03D4gl	22:14:44.183	-17:31:44.36	2966	Keck/LRIS	SNIa	0.571	gal
SNLS-04D1ag	02:24:41.125	-04:17:19.66	2641	VLT/FORS1	SNIa	0.557	gal
SNLS-04D1aj	02:25:53.982	-04:59:40.50	2641	VLT/FORS1	SNIa*	0.72	SN
SNLS-04D1ak	02:27:33.399	-04:19:38.73	2641	VLT/FORS1	SNIa*	0.526	gal
SNLS-04D2ac	10:00:18.923	+02:41:21.63	2641	VLT/FORS1	SNIa*	0.348	gal
SNLS-04D2ae	10:01:52.361	+02:13:21.27	3026	Gem/GMOS	SNIa	0.843	gal
SNLS-04D2al	10:01:52.482	+02:09:51.25	2641	VLT/FORS1	SNIa	0.84	SN
SNLS-04D2an	10:00:52.332	+02:02:28.73	2641	VLT/FORS1	SNIa	0.62	SN
SNLS-04D2bt	09:59:32.725	+02:14:53.07	3085	VLT/FORS1	SNIa	0.220	gal

Table 7. continued.

Name	RA(2000)	Dec(2000)	Obs. date ^a	Tel./Inst. ^b	Spectral type ^c	z^d	z source
SNLS-04D2ca	10:01:20.514	+02:20:21.76	2641	VLT/FORS1	SN Ia	0.83	SN
SNLS-04D2cf	10:01:56.110	+01:52:46.40	3086	VLT/FORS1	SN Ia	0.369	gal
SNLS-04D2cw	10:01:22.787	+02:11:55.31	3085	VLT/FORS1	SN Ia	0.568	gal
SNLS-04D2fp	09:59:28.162	+02:19:15.58	2641	VLT/FORS1	SN Ia	0.415	gal
SNLS-04D2fs	10:00:22.110	+01:45:55.70	2641	VLT/FORS1	SN Ia	0.357	gal
SNLS-04D2gb	10:02:22.676	+01:53:39.34	3117	Keck/LRIS	SN Ia	0.43	SN
SNLS-04D2gc	10:01:39.281	+01:52:59.36	3118	Keck/LRIS	SN Ia	0.521	gal
SNLS-04D2gp	09:59:20.400	+02:30:31.88	3116	VLT/FORS1	SN Ia	0.71	SN
SNLS-04D2iu	10:01:13.221	+02:24:53.91	3139	VLT/FORS1	SN Ia*	0.69	SN
SNLS-04D2ja	09:58:48.519	+01:46:18.64	3139	VLT/FORS1	SN Ia*	0.74	SN
SNLS-04D3bf	14:17:45.096	+52:28:04.31	3054	Gem/GMOS	SN Ia	0.156	gal
SNLS-04D3co	14:17:50.030	+52:57:48.95	3117	Keck/LRIS	SN Ia	0.62	SN
SNLS-04D3cp	14:20:23.954	+52:49:15.45	3119	Keck/LRIS	SN Ia	0.83	SN
SNLS-04D3cy	14:18:12.452	+52:39:30.40	3115	Keck/DMOS	SN Ia	0.643	gal
SNLS-04D3dd	14:17:48.411	+52:28:14.57	3122	Gem/GMOS	SN Ia	1.01	SN
SNLS-04D3df	14:18:10.042	+52:16:39.85	3117	Keck/LRIS	SN Ia	0.47	SN
SNLS-04D3do	14:17:46.113	+52:16:03.36	3117	Keck/LRIS	SN Ia	0.61	SN
SNLS-04D3ez	14:19:07.894	+53:04:19.17	3118	Keck/LRIS	SN Ia	0.263	gal
SNLS-04D3fk	14:18:26.198	+52:31:42.74	3118	Keck/LRIS	SN Ia	0.358	gal
SNLS-04D3fq	14:16:57.902	+52:22:46.46	3123	Gem/GMOS	SN Ia	0.73	SN
SNLS-04D3gt	14:22:32.611	+52:38:49.30	3149	Keck/LRIS	SN Ia*	0.451	gal
SNLS-04D3gx	14:20:13.666	+52:16:58.33	3147	Gem/GMOS	SN Ia*	0.91	SN
SNLS-04D3hn	14:22:06.908	+52:13:43.00	3148	Gem/GMOS	SN Ia	0.552	gal
SNLS-04D3is	14:16:51.968	+52:48:45.70	3149	Keck/LRIS	SN Ia*	0.71	SN
SNLS-04D3ki	14:19:34.598	+52:17:32.61	3149	Keck/LRIS	SN Ia*	0.930	gal
SNLS-04D3kr	14:16:35.943	+52:28:44.02	3173	Gem/GMOS	SN Ia	0.337	gal
SNLS-04D3ks	14:22:33.479	+52:11:07.44	3149	Keck/LRIS	SN Ia*	0.752	gal
SNLS-04D3lp	14:19:50.911	+52:30:11.88	3153	Gem/GMOS	SN Ia*	0.983	gal
SNLS-04D3lu	14:21:08.009	+52:58:29.74	3180	Gem/GMOS	SN Ia	0.822	gal
SNLS-04D3mk	14:19:25.768	+53:09:49.48	3176	Gem/GMOS	SN Ia	0.813	gal
SNLS-04D3ml	14:16:39.095	+53:05:35.89	3177	Gem/GMOS	SN Ia	0.95	SN
SNLS-04D3nc	14:16:18.224	+52:16:26.09	3200	Gem/GMOS	SN Ia*	0.817	gal
SNLS-04D3nh	14:22:26.729	+52:20:00.92	3180	Gem/GMOS	SN Ia	0.340	gal
SNLS-04D3nq	14:20:19.193	+53:09:15.90	3201	Gem/GMOS	SN Ia	0.22	SN
SNLS-04D3nr	14:22:38.526	+52:38:55.89	3202	Gem/GMOS	SN Ia*	0.96	SN
SNLS-04D3ny	14:18:56.332	+52:11:15.06	3197	Gem/GMOS	SN Ia	0.81	SN
SNLS-04D3oe	14:19:39.381	+52:33:14.21	3198	Gem/GMOS	SN Ia	0.756	gal
SNLS-04D4an	22:15:57.119	-17:41:43.93	3200	VLT/FORS1	SN Ia	0.613	gal
SNLS-04D4bk	22:15:07.681	-18:03:36.79	3200	VLT/FORS1	SN Ia*	0.84	SN
SNLS-04D4bq	22:14:49.391	-17:49:39.37	3203	VLT/FORS1	SN Ia	0.55	SN
SNLS-04D4dm	22:15:25.470	-17:14:42.71	3206	Gem/GMOS	SN Ia	0.811	gal
SNLS-04D4dw	22:16:44.667	-17:50:02.38	3206	VLT/FORS1	SN Ia	0.96	SN

^a Date of spectroscopic observations (JD 2 450 000+).^b Telescope and instrument with which the spectrum was acquired.^c See Sect. 2.2 for definitions.^d SN spectrum (SN) or host galaxy spectrum (gal). $\delta z \sim 0.01$ when from SN spectrum, ~ 0.001 when from host galaxy spectrum.

Table 8. Nearby type Ia supernovae.

Name	z^a	Bands	m_B^*	s	c	μ_B^b	Phot. ref. ^c
1990af	0.050	BV	17.723 ± 0.006	0.737 ± 0.001	-0.001 ± 0.009	36.632 ± 0.045	(H96)
1990O	0.031	BV	16.196 ± 0.023^d	1.035 ± 0.033^d	0.017 ± 0.023^d	35.532 ± 0.091	(H96)
1992ae	0.075	BV	18.392 ± 0.037^d	0.939 ± 0.021^d	-0.023 ± 0.025^d	37.642 ± 0.049	(H96)
1992ag	0.026	BV	16.241 ± 0.021^d	1.030 ± 0.027^d	0.155 ± 0.018^d	35.353 ± 0.094	(H96)
1992aq	0.101	BV	19.299 ± 0.028^d	0.839 ± 0.032^d	-0.048 ± 0.020^d	38.437 ± 0.055	(H96)
1992bc	0.020	BV	15.086 ± 0.007	1.033 ± 0.007	-0.031 ± 0.008	34.494 ± 0.111	(H96)
1992bh	0.045	BV	17.592 ± 0.016	0.985 ± 0.016	0.095 ± 0.014	36.728 ± 0.057	(H96)
1992bl	0.043	BV	17.275 ± 0.033^d	0.784 ± 0.016^d	-0.014 ± 0.020^d	36.276 ± 0.059	(H96)
1992bo	0.018	BV	15.753 ± 0.012	0.739 ± 0.006	0.055 ± 0.011	34.576 ± 0.121	(H96)
1992bp	0.079	BV	18.281 ± 0.011	0.873 ± 0.014	-0.043 ± 0.012	37.465 ± 0.041	(H96)
1992br	0.088	BV	19.398 ± 0.073^d	0.650 ± 0.029^d	0.032 ± 0.037^d	38.121 ± 0.046	(H96)
1992bs	0.063	BV	18.177 ± 0.041^d	1.001 ± 0.018^d	-0.034 ± 0.019^d	37.540 ± 0.046	(H96)
1992P	0.026	BV	16.037 ± 0.018^d	1.139 ± 0.084^d	-0.005 ± 0.018^d	35.565 ± 0.141	(H96)
1993ag	0.050	BV	17.799 ± 0.014	0.915 ± 0.018	0.096 ± 0.017	36.827 ± 0.060	(H96)
1993B	0.071	BV	18.377 ± 0.054^d	0.988 ± 0.022^d	0.041 ± 0.026^d	37.604 ± 0.048	(H96)
1993H	0.025	BV	16.735 ± 0.017	0.699 ± 0.012	0.250 ± 0.015	35.192 ± 0.092	(H96, A04)
1993O	0.053	BV	17.614 ± 0.011	0.901 ± 0.010	-0.014 ± 0.011	36.794 ± 0.047	(H96)
1994M	0.024	BV	16.205 ± 0.041^d	0.854 ± 0.019^d	0.040 ± 0.022^d	35.228 ± 0.094	(R99)
1994S	0.016	BV	14.760 ± 0.017	1.018 ± 0.026	0.016 ± 0.017	34.071 ± 0.146	(R99)
1995ac	0.049	BV	17.026 ± 0.009	1.042 ± 0.013	0.010 ± 0.010	36.383 ± 0.051	(R99, A04)
1995bd	0.016	BV	15.246 ± 0.009	0.992 ± 0.009	0.293 ± 0.008	34.083 ± 0.138	(R99, A04)
1996ab	0.125	BV	19.525 ± 0.027^d	0.957 ± 0.033^d	-0.074 ± 0.015^d	38.885 ± 0.049	(R99)
1996bl	0.035	BV	16.611 ± 0.010	0.983 ± 0.015	0.037 ± 0.011	35.837 ± 0.069	(R99)
1996bo	0.016	UBV	15.816 ± 0.006	0.881 ± 0.003	0.343 ± 0.007	34.405 ± 0.133	(R99, A04)
1996bv	0.017	BV	15.380 ± 0.019^d	0.989 ± 0.024^d	0.225 ± 0.009^d	34.319 ± 0.133	(R99)
1996C	0.030	BV	16.636 ± 0.029^d	1.045 ± 0.111^d	0.122 ± 0.010^d	35.822 ± 0.210	(R99)
1997dg	0.030	UBV	16.821 ± 0.014^d	0.917 ± 0.024^d	0.005 ± 0.010^d	35.994 ± 0.080	(J02)
1997Y	0.017	UBV	15.284 ± 0.020^d	0.916 ± 0.024^d	0.008 ± 0.014^d	34.452 ± 0.136	(J02)
1998ab	0.028	UBV	16.048 ± 0.010	0.938 ± 0.008	0.071 ± 0.007	35.150 ± 0.079	(J02)
1998dx	0.054	UBV	17.660 ± 0.055^d	0.733 ± 0.039^d	-0.028 ± 0.019^d	36.606 ± 0.054	(J02)
1998eg	0.024	UBV	16.089 ± 0.009	0.940 ± 0.029	0.036 ± 0.012	35.250 ± 0.102	(J02)
1998V	0.017	UBV	15.094 ± 0.011^d	0.909 ± 0.016^d	0.030 ± 0.006^d	34.216 ± 0.128	(J02)
1999aw	0.039	BV	16.732 ± 0.005	1.205 ± 0.008	0.044 ± 0.006	36.284 ± 0.057	(S02)
1999cc	0.032	UBV	16.791 ± 0.009	0.840 ± 0.013	0.043 ± 0.010	35.789 ± 0.074	(J02)
1999ek	0.018	UBV	15.584 ± 0.004	0.892 ± 0.007	0.153 ± 0.005	34.489 ± 0.124	(J02, K04b)
1999gp	0.026	UBV	16.005 ± 0.004	1.104 ± 0.007	0.083 ± 0.004	35.342 ± 0.084	(J02, K01)
2000ca	0.025	UBV	15.510 ± 0.007	1.006 ± 0.013	-0.066 ± 0.006	34.931 ± 0.091	(K04a)
2000cf	0.036	UBV	17.091 ± 0.027^d	0.868 ± 0.024^d	0.054 ± 0.013^d	36.113 ± 0.066	(J02)
2000cn	0.023	UBV	16.544 ± 0.007	0.732 ± 0.006	0.190 ± 0.006	35.146 ± 0.094	(J02)
2000dk	0.016	UBV	15.323 ± 0.005	0.724 ± 0.006	0.052 ± 0.005	34.129 ± 0.133	(J02)
2000fa	0.022	UBV	15.832 ± 0.014	0.953 ± 0.010	0.081 ± 0.009	34.941 ± 0.101	(J02)
2001ba	0.031	BV	16.182 ± 0.006	1.000 ± 0.011	-0.043 ± 0.008	35.558 ± 0.075	(K04a)
2001cn	0.015	UBV	15.271 ± 0.013^d	0.911 ± 0.012^d	0.208 ± 0.007^d	34.118 ± 0.142	(K04b)
2001cz	0.017	UBV	15.035 ± 0.006	1.004 ± 0.010	0.120 ± 0.007	34.162 ± 0.127	(K04b)

^a CMB-centric redshift.

^b Computed with $H_0 = 70 \text{ km s}^{-1} \text{ Mpc}^{-1}$. Uncertainty only accounts for photometric uncertainties.

^c Photometry references: H96: Hamuy et al. (1996), R99: Riess et al. (1999), K01: Krisciunas et al. (2001), J02: Jha (2002), A04: Altavilla et al. (2004), K04a: Krisciunas et al. (2004a), K04b: Krisciunas et al. (2004b), S02: Strolger et al. (2002).

^d First photometric measurement after B -band maximum, see discussion in Sect. 5.2.

Table 9. SNLS type Ia supernovae.

Name	z^a	Bands	m_B^*	stretch ^b	color ^b	μ_B^c
SNLS-03D1au	0.504	riz	22.978 ± 0.010	1.124 ± 0.019	0.030 ± 0.018	42.429 ± 0.039
SNLS-03D1aw	0.582	riz	23.599 ± 0.020	1.002 ± 0.024	0.018 ± 0.030	42.881 ± 0.054
SNLS-03D1ax	0.496	riz	22.957 ± 0.011	0.899 ± 0.010	-0.044 ± 0.021	42.180 ± 0.038
SNLS-03D1bp	0.346	riz	22.465 ± 0.014	0.880 ± 0.007	0.143 ± 0.017	41.367 ± 0.021
SNLS-03D1cm	0.870	griz	24.469 ± 0.066	1.173 ± 0.061	-0.035 ± 0.143	44.095 ± 0.301
SNLS-03D1co	0.679	griz	24.094 ± 0.033	0.975 ± 0.032	-0.021 ± 0.047	43.398 ± 0.088
SNLS-03D1ew	0.868	griz	24.359 ± 0.078	1.028 ± 0.040	-0.102 ± 0.169	43.871 ± 0.344
SNLS-03D1fc	0.331	griz	21.800 ± 0.005	0.937 ± 0.005	0.042 ± 0.004	40.946 ± 0.013
SNLS-03D1fl	0.688	griz	23.629 ± 0.015	0.999 ± 0.024	-0.070 ± 0.021	43.046 ± 0.049
SNLS-03D1fq	0.800	griz	24.519 ± 0.030	0.806 ± 0.052	0.027 ± 0.030	43.490 ± 0.090
SNLS-03D1gt	0.548	griz	24.119 ± 0.048	0.856 ± 0.042	0.244 ± 0.050	42.825 ± 0.080
SNLS-03D3af	0.532	gri	23.470 ± 0.027	0.907 ± 0.023	0.029 ± 0.031	42.592 ± 0.083
SNLS-03D3aw	0.449	griz	22.552 ± 0.016	0.955 ± 0.013	-0.048 ± 0.019	41.866 ± 0.044
SNLS-03D3ay	0.371	griz	22.201 ± 0.016	0.968 ± 0.010	-0.018 ± 0.014	41.488 ± 0.030
SNLS-03D3ba	0.291	griz	22.049 ± 0.034	1.036 ± 0.021	0.263 ± 0.015	40.999 ± 0.033
SNLS-03D3bh	0.249	griz	21.132 ± 0.018	0.993 ± 0.008	-0.090 ± 0.013	40.571 ± 0.020
SNLS-03D3cc	0.463	gri	22.558 ± 0.111	1.074 ± 0.031	-0.070 ± 0.050	42.089 ± 0.034
SNLS-03D3cd	0.461	gri	22.562 ± 0.017	1.131 ± 0.034	0.025 ± 0.011	42.031 ± 0.058
SNLS-03D4ag	0.285	griz	21.237 ± 0.005	1.059 ± 0.005	-0.061 ± 0.004	40.731 ± 0.015
SNLS-03D4at	0.633	griz	23.746 ± 0.020	0.989 ± 0.029	-0.060 ± 0.030	43.133 ± 0.064
SNLS-03D4au ^d	0.468	griz	23.856 ± 0.020	1.000 ± 0.030	0.291 ± 0.034	42.708 ± 0.069
SNLS-03D4bc ^d	0.572	griz	24.596 ± 0.061	0.774 ± 0.048	0.025 ± 0.078	43.521 ± 0.135
SNLS-03D4cn	0.818	griz	24.652 ± 0.051	0.743 ± 0.059	0.023 ± 0.158	43.532 ± 0.304
SNLS-03D4cx	0.949	griz	24.504 ± 0.083	0.882 ± 0.019	0.080 ± 0.124	43.507 ± 0.272
SNLS-03D4cy	0.927	griz	24.718 ± 0.109	1.031 ± 0.052	-0.305 ± 0.174	44.553 ± 0.380
SNLS-03D4cz	0.695	griz	24.019 ± 0.036	0.729 ± 0.024	-0.069 ± 0.043	43.023 ± 0.086
SNLS-03D4dh	0.627	griz	23.389 ± 0.011	1.061 ± 0.013	0.028 ± 0.016	42.746 ± 0.035
SNLS-03D4di	0.905	griz	24.288 ± 0.068	1.103 ± 0.041	0.029 ± 0.120	43.708 ± 0.258
SNLS-03D4dy	0.604	griz	23.313 ± 0.010	1.056 ± 0.001	0.122 ± 0.015	42.515 ± 0.029
SNLS-03D4fd	0.791	griz	24.212 ± 0.025	0.919 ± 0.033	0.028 ± 0.044	43.353 ± 0.076
SNLS-03D4gf	0.581	griz	23.351 ± 0.013	1.009 ± 0.026	-0.056 ± 0.024	42.761 ± 0.047
SNLS-03D4gg	0.592	griz	23.403 ± 0.024	0.966 ± 0.049	0.062 ± 0.035	42.562 ± 0.090
SNLS-03D4gl	0.571	griz	23.269 ± 0.026	0.957 ± 0.033	0.030 ± 0.028	42.465 ± 0.070
SNLS-04D1ag	0.557	griz	23.003 ± 0.011	0.944 ± 0.013	-0.182 ± 0.017	42.511 ± 0.029
SNLS-04D1aj	0.721	griz	23.901 ± 0.030	1.074 ± 0.067	0.072 ± 0.038	43.209 ± 0.106
SNLS-04D1ak	0.526	griz	23.631 ± 0.028	0.824 ± 0.021	0.018 ± 0.033	42.644 ± 0.055
SNLS-04D2cf	0.369	griz	22.340 ± 0.007	0.895 ± 0.003	0.002 ± 0.010	41.485 ± 0.016
SNLS-04D2fp	0.415	griz	22.528 ± 0.010	0.964 ± 0.010	0.006 ± 0.015	41.772 ± 0.027
SNLS-04D2fs	0.357	griz	22.422 ± 0.008	0.942 ± 0.009	0.128 ± 0.008	41.441 ± 0.018
SNLS-04D2gb	0.430	griz	22.796 ± 0.018	0.777 ± 0.013	-0.008 ± 0.025	41.776 ± 0.038
SNLS-04D2gc	0.521	griz	23.321 ± 0.014	1.065 ± 0.024	0.185 ± 0.022	42.439 ± 0.054
SNLS-04D2gp	0.707	griz	24.151 ± 0.047	0.801 ± 0.002	-0.052 ± 0.060	43.237 ± 0.129
SNLS-04D2iu	0.691	griz	24.258 ± 0.048	0.800 ± 0.035	0.074 ± 0.056	43.144 ± 0.136
SNLS-04D2ja	0.741	griz	24.098 ± 0.045	0.945 ± 0.036	-0.067 ± 0.043	43.427 ± 0.117
SNLS-04D3co	0.620	griz	23.781 ± 0.022	0.895 ± 0.017	-0.064 ± 0.030	43.030 ± 0.060
SNLS-04D3cp	0.830	griz	24.235 ± 0.063	1.110 ± 0.035	-0.448 ± 0.180	44.414 ± 0.347
SNLS-04D3cy	0.643	griz	23.798 ± 0.021	0.963 ± 0.016	0.017 ± 0.029	43.023 ± 0.059
SNLS-04D3dd	1.010	griz	25.120 ± 0.192	1.088 ± 0.074	-0.071 ± 0.205	44.673 ± 0.533
SNLS-04D3df	0.470	griz	23.465 ± 0.010	0.730 ± 0.010	0.060 ± 0.017	42.268 ± 0.032

Table 9. continued.

Name	z^a	Bands	m_B^*	stretch ^b	color ^b	μ_B^c
SNLS-04D3do	0.610	griz	23.574 ± 0.014	0.862 ± 0.013	-0.079 ± 0.019	42.796 ± 0.039
SNLS-04D3ez	0.263	griz	21.678 ± 0.004	0.895 ± 0.006	0.091 ± 0.003	40.682 ± 0.013
SNLS-04D3fk	0.358	griz	22.532 ± 0.005	0.913 ± 0.005	0.149 ± 0.006	41.474 ± 0.013
SNLS-04D3fq	0.730	griz	24.128 ± 0.026	0.900 ± 0.014	-0.002 ± 0.037	43.287 ± 0.075
SNLS-04D3gt	0.451	griz	23.235 ± 0.010	0.953 ± 0.010	0.276 ± 0.016	42.038 ± 0.030
SNLS-04D3gx	0.910	griz	24.708 ± 0.094	0.952 ± 0.047	-0.202 ± 0.163	44.259 ± 0.346
SNLS-04D3hn	0.552	griz	23.475 ± 0.011	0.898 ± 0.011	0.106 ± 0.017	42.461 ± 0.035
SNLS-04D3is	0.710	griz	24.256 ± 0.027	0.972 ± 0.002	0.220 ± 0.038	43.176 ± 0.077
SNLS-04D3ki	0.930	griz	24.871 ± 0.126	0.901 ± 0.039	-0.256 ± 0.194	44.430 ± 0.430
SNLS-04D3kr	0.337	griz	21.967 ± 0.003	1.064 ± 0.004	0.072 ± 0.003	41.259 ± 0.010
SNLS-04D3ks	0.752	griz	23.882 ± 0.035	1.013 ± 0.037	0.026 ± 0.043	43.170 ± 0.090
SNLS-04D3lp	0.983	griz	24.925 ± 0.168	0.831 ± 0.049	0.022 ± 0.211	43.941 ± 0.496
SNLS-04D3lu	0.822	griz	24.342 ± 0.040	0.950 ± 0.028	0.019 ± 0.116	43.544 ± 0.218
SNLS-04D3ml	0.950	griz	24.552 ± 0.082	1.182 ± 0.015	0.117 ± 0.122	43.954 ± 0.268
SNLS-04D3nc	0.817	griz	24.271 ± 0.048	1.111 ± 0.064	0.062 ± 0.140	43.652 ± 0.254
SNLS-04D3nh	0.340	griz	22.137 ± 0.004	1.011 ± 0.006	0.089 ± 0.004	41.323 ± 0.012
SNLS-04D3nr	0.960	griz	24.542 ± 0.075	0.922 ± 0.045	0.070 ± 0.110	43.622 ± 0.234
SNLS-04D3ny	0.810	griz	24.272 ± 0.050	1.005 ± 0.084	-0.065 ± 0.152	43.691 ± 0.301
SNLS-04D3oe	0.756	griz	24.069 ± 0.026	0.783 ± 0.028	-0.259 ± 0.033	43.453 ± 0.058
SNLS-04D4an	0.613	griz	24.022 ± 0.023	0.823 ± 0.025	0.064 ± 0.025	42.961 ± 0.061
SNLS-04D4bk	0.840	griz	24.314 ± 0.037	1.050 ± 0.051	0.142 ± 0.098	43.475 ± 0.185
SNLS-04D4bq	0.550	griz	23.362 ± 0.020	0.995 ± 0.029	0.112 ± 0.027	42.487 ± 0.056
SNLS-04D4dm	0.811	griz	24.390 ± 0.044	1.000 ± 0.057	-0.161 ± 0.150	43.950 ± 0.264
SNLS-04D4dw	0.961	griz	24.566 ± 0.093	0.962 ± 0.058	-0.117 ± 0.138	44.000 ± 0.290

^a Heliocentric redshift.^b See Sect. 5.1 for description.^c Computed with $H_0 = 70 \text{ km s}^{-1} \text{ Mpc}^{-1}$. Uncertainty only accounts for photometric uncertainties.^d Not included in the final cosmological fits.